Title:

Bipolar and schizophrenia risk gene *AKAP11* encodes an autophagy receptor coupling the regulation of PKA kinase network homeostasis to synaptic transmission

You-Kyung Lee[1,2,11], Cong Xiao[1,2,11], Xiaoting Zhou[1,2], Le Wang[3], Meghan G. McReynolds[4,5], Xian Han[4,5], Zhiping Wu[4,5], Eric Purisic[2,6], Henry Kim[1,2], Xianting Li[1,2], Zhiping Pang[3], Jinye Dai[6], Junmin Peng[4,5], Nan Yang[2,7,8,9], Zhenyu Yue[1,2,10,*]

[1]Department of Neurology, The Friedman Brain Institute, Icahn School of Medicine at Mount Sinai, New York, NY 10029.

[2]Department of Neuroscience, The Friedman Brain Institute, Icahn School of Medicine at Mount Sinai, New York, NY 10029.

[3]Child Health Institute of New Jersey and Department of Neuroscience and Cell Biology, Robert Wood Johnson Medical School, Rutgers University, New Brunswick, NJ, 08901, USA.

[4]Department of Structural Biology, St. Jude Children's Research Hospital, Memphis, TN 38105, USA.

[5]Department of Developmental Neurobiology, St. Jude Children's Research Hospital, Memphis, TN 38105, USA.

[6]Department of Pharmacological Sciences, The Friedman Brain Institute, Icahn School of Medicine at Mount Sinai, New York, NY 10029.

[7]Black Family Stem Cell Institute, Icahn School of Medicine at Mount Sinai, New York, NY 10029, USA.

[8]Alper Center for Neurodevelopment and Regeneration, Icahn School of Medicine at Mount Sinai, New York, NY 10029, USA.

[9]Institute for Regenerative Medicine, Icahn School of Medicine at Mount Sinai, New York, NY 10029, USA.

27 [10]Center for Parkinson's Disease Neurobiology

28 [11]These authors contributed equally: You-Kyung Lee, Cong Xiao.

Abstract

Human genomic studies have identified protein-truncating variants in *AKAP11* associated with both bipolar disorder (BD) and schizophrenia (SCZ), implicating a shared disease mechanism driven by loss-of-function. AKAP11, a protein kinase A (PKA) adaptor, plays a key role in degrading the PKA-RI complex through selective autophagy. However, the neuronal functions of AKAP11 and the impact of its loss-of-function remains largely uncharacterized. Through multi-omics approaches, cell biology, and electrophysiology analysis in mouse models and human induced neurons, we delineated a central role of AKAP11 in coupling PKA kinase network regulation to synaptic transmission. Loss of AKAP11 distorted compartment-specific PKA and GSK3α/β activities and impaired cellular functions that significantly overlap with pathways associated with BD and SCZ. Moreover, we identified interactions between AKAP11, the PKA-RI adaptor SPHKAP, and the ER-resident autophagy-related proteins VAPA/B, which co-adapt and mediate PKA-RI complex degradation in neurons. Notably, AKAP11 deficiency impaired neurotransmission, providing key insights into the mechanism underlying *AKAP11*-associated psychiatric diseases.

Introduction

A meta-analysis combining exome sequencing uncovered a link of rare protein-truncating variants (PTVs) to increased risk of bipolar disorder (BD) and identified *AKAP11* as a definitive risk gene for BD shared with schizophrenia (SCZ)[1]. Two independent meta-analyses of whole exome sequencing also revealed that *AKAP11*-coding or truncating variants enhanced the risk of SCZ across diverse human populations[2,3]. Thus, the human genetic evidence demonstrates *AKAP11* as a common risk gene for both BD and SCZ and implicates a potential disease mechanism involving the loss-of-function in the AKAP11. However, the biology and pathophysiology of AKAP11 in the central nervous system (CNS) remains poorly understood.

AKAP11 (A-kinase Anchoring Protein 11), known also as AKAP220, is a member of the protein family that anchors Protein Kinase A (PKA) complex to specific subcellular locations, modulating PKA and GSK-3β activity[4–8]. We previously reported a cellular function of AKAP11 as an autophagy receptor, which mediates the selective degradation of the regulatory RI subunits (RIα and RIβ) of PKA, while sparing RII subunits, through binding autophagy protein LC3 and controls PKA activity[9]. We recently documented the conserved autophagy function of AKAP11 in human neurons and demonstrated a critical role of AKAP11 in maintaining the homeostasis of PKA-RI protein complex in the soma and neurites through autophagy degradation[10]. Interestingly, *Akap11* knock-out mice exhibit behavioral abnormalities in electroencephalogram (EEG) recording in common with symptoms of SCZ[11], supporting potential synaptic dysfunction[12]. Given the notion that neuronal autophagy regulates synaptic function[13–19], it raises a question for how AKAP11-mediated autophagy is linked to the regulation of synaptic activity. The knowledge of the mechanism whereby AKAP11 controls PKA-RI complex homeostasis and synaptic functions in neurons is expected to provide insight into the pathogenesis of BD and SCZ.

Here we reported an interdisciplinary study of AKAP11 neuronal function and the consequence of the loss-of-function in AKAP11 in both genetic mouse models and human induced neurons (iNeurons) by integrating multi-omics, cell biology, and electrophysiology approaches. We observed an extensive distortion of PKA kinase network and altered PKA and GSK3α/β kinase activities in neurons from *AKAP11*-deficient neurons. Furthermore, loss of AKAP11 results in a compartment-specific change of PKA activity in neurons. Our study demonstrated the role of

AKAP11 in coupling PKA kinase network regulation to synaptic transmission. Finally, our data identified a novel autophagy function of AKAP11 in neurons through interacting with the PKA adaptor SPHKAP and the ER-resident autophagy related proteins VAPA/B. Our current report offers a comprehensive view of *AKAP11*-regulated neuronal pathways and insight of the pathogenic mechanisms underlying the psychiatric diseases.

Integrated proteomics identified profound changes of PKA kinase network and synaptic proteins in *AKAP11*-deficient neurons

We previously reported that *AKAP11* knockdown (KD) leads to an increase of protein level in the regulatory subunits RIα and RIβ of PKA in iNeurons[10], confirming its role as autophagy receptor. Here we sought to determine AKAP11-targeted proteins and cellular pathways by performing a systematic search in neurons through integrated proteomics profiling, as we described in the study of autophagy cargo identification[10](Fig. 1a). For this purpose, we established *Akap11*-conditional knock-out (cKO) (Cre-LoxP) and whole-body knock-out (wKO) mice (Extended Data Fig. 1a). Together with human *AKAP11*-KD iNeuron, we conducted quantitative mass spectrometry-based proteomics (Tandem Mass Tag (TMT) and Data-independent Acquisition (DIA))[20–22] and analyzed the changes of proteins and cellular pathways in neurons from mutant mouse brains and iNeurons compared to control neurons. In total, 7427 proteins (54 up-regulated, 124 down-regulated), 5619 proteins (86 up-regulated, 29 down-regulated), and 11392 proteins (175 up-regulated, 13 down-regulated) were detected in *Akap11*-cKO, iNeuron-KD, and wKO datasets, respectively (Fig. 1b,c, Extended Data Fig. 1b and Supplementary Table 1-3).

We next annotated the differential expression of proteins (DEPs) in the *AKAP11*-cKO neurons. For the upregulated DEPs, functional annotation with clusterProfiler[23] identified cAMP-dependent PKA binding related pathways as the dominant GO terms, including protein kinase regulator activity and PKA catalytic subunit binding under the Molecular Function (MF) category. In Cellular Component (CC) category, examples of significantly enriched GO terms include negative regulation of phosphorus metabolic process and negative regulation of kinase activity (Fig. 1d and Extended Data Fig. 1c). Indeed, we observed a significant enrichment of PKA-RIα (log2FoldChange (FC) 1.84) and RIβ (FC 1.88) levels as well as PKA-Cα (FC 0.91) and Cβ (FC 0.92) levels in *Akap11*-cKO dataset, and similar patterns in other two datasets (Fig. 1b,c,e and Extended Data Fig. 1b,d). Furthermore, multiple negative regulators of PKA activity are among the significantly upregulated DEPs in *Akap11*-cKO mouse brains, such as ADRA2A (FC 1.06), PDE4B (FC 1.38), PDE3A (FC 0.80), and PKIB (FC 0.83) (Fig. 1b,e and Extended Data Fig. 1b). ADRA2A inhibits adenyl cyclase (AC), leading to a decrease in protein kinase A (PKA) activity[24–26]. PDE3A and PDE4B inhibit PKA activity by breaking down cAMP, and PDE4B is a major binding partner of DISC1 and a risk gene for SCZ and BD[27–29]. PKIB belongs to cAMP-dependent protein kinase inhibitor family, and it regulates PKA pathway by interacting

110 with the PKA-C subunit[30]. Additionally, we observed an enrichment of SPHKAP (FC 0.57, SD =
111 0.41), which is a PKA-RI subtype-specific anchoring protein[31] (Fig. 1e). The increase of PKA-
112 RIα/β, PKA-C (with a lesser degree than PKA-RI), ADRA2A, and SPHKAP proteins in *Akap11*-
113 cKO brains were validated through immunoblot. The RIα/β proteins were accumulated in large
114 discrete puncta in *Akap11*-deficient neurons as shown through immunofluorescence (IF) imaging
115 (Fig. 1f,g,h).

116 In the downregulated DEPs, the annotation identified neural or synapse-related functions as the
117 primarily affected terms, including synaptic vesicle (SV) membrane, exocytic vesicle membrane,
118 SV, and myelin sheath (CC). Significant GO terms also include regulation of neurotransmitter
119 transport and SV endocytosis in Biological Process (BP). Additionally, G protein activity,
120 GTPase regulator activity, and transmembrane transporter binding are the main GO terms (MF)
121 (Extended Data Fig. 1e). We noticed the downregulation of CREB1 (FC -0.92), a downstream
122 target of PKA signaling pathway[32], and synaptophysin (FC -1.09), a synaptic vesicle (SV)-
123 associated protein important for synaptic trafficking and neurotransmitter release[33]. Additionally,
124 the downregulated expression of calcium/calmodulin-dependent protein kinases, CAMKIIA (FC
125 -0.51) indicates reduced neuronal calcium signaling, which plays a pivotal role in synaptic
126 plasticity and memory formation[34] (Fig. 1b).

127 To verify the changes of synaptic proteins identified in the proteomics analysis, we performed
128 immunoblotting in *Akap11*-cKO brain lysates. We observed that the levels of synaptophysin were
129 decreased in mutant brains (Fig. 1h). Using SynGO[35] to screen the DEPs in *Akap11*-cKO mouse
130 and *AKAP11*-KD iNeuron, we found an enrichment in both pre- and postsynaptic compartments,
131 sharing multiple "sub-synaptic" terms, including regulation of synapse assembly, SV exocytosis
132 and endocytosis, postsynaptic membrane neurotransmitter receptor levels, and chemical synaptic
133 transmission (Extended Data Fig. 2a). The above evidence suggests that *AKAP11*-deficiency
134 affects synaptic homeostasis and perhaps synaptic transmission.

135 We next performed transcriptome analysis of *Akap11*-cKO mouse brains. The number of
136 differential expression genes (DEGs) in mutant mice is significantly less than that of DEPs
137 (Extended Data Fig. 2b). Even with diminishing *Akap11* transcripts, *Akap11*-cKO brains showed
138 little change of mRNA levels coding for PKA complex or its regulators as described above,
139 supporting the regulatory role of AKAP11 in regulating PKA complex proteins post-

transcriptionally. Meanwhile, Gene Set Enrichment Analysis (GSEA)[36,37] indicates the down-regulated DEGs associated with synapse, including pre- and postsynaptic membrane, dendrite development, axonogenesis, actin and filament binding, etc. (Extended Data Fig. 2c).

Furthermore, through a comprehensive platform integrating information on human disease-associated genes and variants (DisGeNET)[38], we found remarkably SCZ as the top ranked disease based on the protein count (Fig. 1i), suggesting a convergence of AKAP11-regulated cellular functions and potential SCZ-inflicted disease pathways.

Identification of PKA subunits as central hubs in network modules for synapse formation regulated by AKAP11

To gain an insight of the relationship among cellular pathways/functions affected by the loss-of -function in *AKAP11* as autophagy receptor, we employed the modified Weighted Gene Co-expression Network Analysis (WGCNA)[39,40] to dissect proteomics data from *Akap11*-cKO mouse brains and human *AKAP11*-KD iNeurons. WGCNA construction identified 13 and 18 modules in mutant mouse brains and human iNeurons, respectively (Fig. 2a,e).

In *Akap11*-cKO brain dataset, module ME5 (1146 proteins) and ME4 (106 proteins) (Supplementary Table 4), are top ranked and positively correlated with the trait (mutant) with a *P*-value of 3e-07 and 2e-04, respectively. We found PKA-RIα/β and PKA-Cα/β are the hub proteins in the ME5 based on their highest scores in Peptide Significance (PS) and Module Membership (MM) (Fig. 2b). Interestingly, the GO term analysis reveals that ME5 is highly enriched in endosomal transport, postsynapse organization, synaptic vesicle and neuron to neuron synapse (Fig. 2c). Detailed analysis of "subsynaptic" processes of the ME5 showed the translation at presynapse, regulation of postsynaptic density assembly, SV exocytosis, chemical synaptic transmission, and neurotransmitter receptor localization of postsynaptic specialization membrane (Fig. 2d). In ME4, the proteins GOLPH3, PGM3, SSB, and CHMP2B are hub proteins and involved in protein metabolic process (Extended Data Fig. 3a). GO term analysis shows that ME4 is enriched in protein catabolic process, cytoplasmic translation, and proteasome complex (Extended Data Fig. 3b).

168 In *AKAP11*-KD iNeuron dataset, the ME15 (482 proteins) and ME13 (344 proteins) are the top
169 two positively correlated modules (Supplementary Table 5). Similarly, PKA-RIα/β subunits were
170 identified as hub proteins followed by PKA-Cα/β in the ME15 (significant PS and MM), while
171 the ME15 showed the enrichment in macroautophagy, glutamatergic synapse, transport vesicle,
172 and protein polymerization or depolymerization (Fig. 2f,g). In ME13, NUP35, NMT2, MTM1,
173 and BCL2 are hub proteins, which are involved in endomembrane system, while GO term
174 analysis reveals the association of ME13 with endosomal transport, early endosome, and
175 lysosomal membrane (Extended Data Fig. 3c,d). Therefore, the data from both mouse brains and
176 human iNeuron show a remarkable consensus where PKA subunits are the hub proteins in the
177 synapse-related modules. The results demonstrate a functional accordance of PKA signaling
178 pathways with synaptic function, which are co-regulated by AKAP11. Moreover, the data
179 indicated a functional correlation of PKA signaling, autophagy, and vesicle trafficking pathway
180 through AKAP11, in agreement with our early observation[9].

181 We next employed STRING[41] to analyze protein-protein interaction (PPI) network of the PKA-
182 centered protein module (ME5) (only FDR < 0.05 proteins). While PKA-RIα/β as the most
183 significant DEPs (increase) in *Akap11*-cKO brains and as the main hub proteins (upregulated) in
184 the ME5 (Fig. 1b), they are found as the central nodes in the PPI network, which interact with
185 MAPT, GSK3A, ARFGEF1, ANK3, EZR, NDUFA9, and PRKAB1 (Fig. 2h). Indeed, those
186 interacting proteins are the known PKA targets or mediators of PKA signaling pathways in
187 various cellular functions or neural activity[6,31,42–50]. The evidence indicated a significant
188 alteration of PKA signaling network, including PKA holoenzyme subunits, upstream regulators,
189 and downstream targets, in *AKAP11*-deficient neurons.

190

191 **Disruption of neuronal AKAP11 altered protein phosphorylation landscape and**
192 **compartment-specific PKA activities**

193 The increase of protein levels in PKA regulatory subunits RIα/β as well as in multiple PKA
194 activity inhibitors (Fig. 1e,f,h and Extended Data Fig. 1d) led to a hypothesis that PKA activity is
195 disrupted in *AKAP11*-deficient neurons. To test the hypothesis, we analyzed phosphoproteomics
196 data obtained from the brains of *Akap11*-cKO mice and determined changes of potential PKA
197 phosphorylation sites. We identified 289 differentially abundant phosphoprotein sites (DAPPSs)

198 between the *Akap11*-cKO and control brain lysates (91 upregulated and 198 downregulated) (Fig.
199 3a and Supplementary Table 6). Strikingly, given the finding of genetic risk of *AKAP11* variants
200 in SCZ and BD, the enrichment analysis of the DAPPSs corresponding proteins through the
201 DisGeNET[38] database reveals an enrichment of diseases such as SCZ, BD, intellectual disability,
202 neurodevelopmental disorders, and unipolar depression in *Akap11*-cKO brains (Fig. 3b).

203 We next employed a comprehensive pipeline PhosR[51] to delineate the kinase and substrate
204 relationship. The PhosR utilizes the PhosphoSitePlus[52] as a reference database and a set of tools
205 and methodologies implemented in R to allow the comprehensive analysis of the
206 phosphoproteomic data[53]. The predicted top three phosphorylation sites of the corresponding
207 kinases are shown in a heatmap (Extended Data Fig. 4a). Additionally, we analyzed the top 400
208 predicted PKA phosphosites and found 39 significantly downregulated DAPPSs and 41
209 phosphorylation sites with a trend of decrease (Extended Data Fig. 4b). After normalizing against
210 the levels of corresponding proteins from proteomics results (Supplementary Table 1), we
211 identified 22 downregulated DAPPSs (Fig. 3c) associated potentially with PKA activity in
212 *Akap11*-cKO neurons.

213 In a parallel analysis, we mapped the phosphoproteomic data against the PKA consensus
214 substrates from PhosphoSitePlus[52] and identified 30 phosphosites (of which 20 were found as
215 predicted PKA phosphosites from the PhosR analysis). Among them, 6 show a trend of increase
216 while 9 display a trend of reduction (FDR <0.2, 1*SD) (Extended Data Fig. 4c).

217 To validate PKA activity changes, we first assessed the protein levels of PKA subunits in cytosol
218 and synaptosome fractions and found an increase of PKA-C and PKA-RI in both fractions from
219 *Akap11*-cKO brain lysates by immunoblot. We noticed that the increase of RIβ was much greater
220 in cytosol (6.41-fold) than in synaptosome (1.47-fold), while PKA-C changed in the opposite
221 direction within cytosolic (1.52-fold) and synaptosome (3.09-fold) (Fig. 3d). We then performed
222 an enzyme-linked immunosorbent assay (ELISA) to analyze PKA activity[54,55]. The assay
223 sensitivity was verified using forskolin (FSK, a PKA activator) and H89 (a PKA inhibitor)
224 (Extended Data Fig. 4d). Remarkably, the ELISA results showed a reduction PKA activity in the
225 cytosol but an increase in the synaptosome (Fig. 3e). The increase of PKA activity in the
226 synaptosomes were supported by increased phosphorylation of the PKA substrate p-GluA1^{S845}
227 and of PKA-Cα^{T197} (Fig. 3f and Extended Data Fig.4e). The reduced PKA activity in the cytosol

228 occurred in different brain regions, such as the cerebral cortex and hippocampus, in *Akap11*-
229 wKO mice (Extended Data Fig. 4f). These findings indicate that the loss of AKAP11 induces
230 compartment-specific alterations of PKA activities. It is conceivable that the greater elevation of
231 regulatory subunit of PKA-RI levels causes repression of PKA activity in the cytosol, while the
232 increase of PKA-C in the synaptosome fraction, which escape from binding to a moderate
233 enhancement of PKA-RI, could result in the increase of PKA activity in synapse.

234 Moreover, we performed the GO term analysis of the 399 predicted PKA substrates based on
235 PhosR (Supplementary Table 7), the top enriched pathways were postsynaptic density and
236 specialization, asymmetric synapse, and neuron spine axon (CC), post-synapse organization and
237 exocytosis (BP), and actin binding (MF) (Fig. 3g and Extended Data Fig. 4g). The SynGO[35]
238 analysis further showed the enrichment of the predicted PKA substrates in structural constituent
239 of postsynapse, regulation of synapse assembly, SV exocytosis and endocytosis, and modulation
240 of chemical synaptic transmission (Fig. 3h). These evidences corroborate the results from
241 WGCNA showing the accordance of PKA network with synaptic activity (Fig. 2c,d,h).

242

243 **Loss-of-function in AKAP11 impaired GSK3α/β kinase activity in neurons**

244 The PhosR further predicted a reduction in the kinase activities of GSK3β, PKC isoforms (α, γ,
245 δ, ι, θ), and CaMKIIα alongside PKA, while AKT1 activity exhibits an increase (Fig. 4a).

246 Because GSK3α/β are known AKAP11-binding proteins[5], we then analyzed GSK3α/β activities
247 using PhosR and examined the specific phosphorylation sites of the kinase as a proxy through
248 immunoblot. From the top 200 predicted GSK3β sites normalized by corresponding protein
249 levels from proteomics results, we identified 17 DAPPSs, which were all downregulated (Fig.
250 4b), suggesting a decrease of GSK3β activity in *Akap11*-cKO neurons. Immunoblot with anti-
251 phospho-GSK3α/β antibodies (Ser21 in GSK3α and Ser9 in GSK3β) showed enhanced
252 phosphorylation levels of GSK3α/β in both cytosolic and synaptosome fractions in *Akap11*-cKO
253 mouse brain (Fig. 4c,e) as well as *Akap11*-whole body KO mouse brains (Extended Data Fig.
254 5a). Our findings revealed that both AKAP11 and GSK3α/β were predominantly distributed in
255 the cytosol relative to synaptosome fractions (Fig. 3d,4e), which aligns with the report that

256 AKAP11directly binds GSK3α/β[5]. These above results demonstrate a reduction of
257 GSK3α/β activities in *AKAP11* deficient neurons.

258 Additionally, we analyzed AKT1 kinase activity based on the normalized predicted top 200
259 AKT1 substrates. We identified 5 DAPPSs, all of which were upregulated. Among the rest of the
260 predicted substrates, many exhibited a trend of increased phosphorylation levels (Fig. 4d).
261 Immunoblot of the p-AKT1 Ser473 with a specific antibody, which detects phosphorylation of
262 Ser 473 within the carboxyl-terminal hydrophobic motif that is required for Akt/PKB
263 activation[56], showed an increase in the cytosolic fraction in *Akap11*-cKO neurons (Fig. 4e). Note
264 that p-AKT1 is nearly undetectable in the synaptosome fraction (Fig. 4e). The results corroborate
265 an increase in AKT1 activity in the cytosol in *Akap11*-cKO neurons. Given that AKT1 can
266 phosphorylate GSK3α (Ser 21) and GSK3β (Ser 9)[57], our data are consistent with an idea that
267 the loss of AKAP11 causes AKT1 activation, leading to the elevated phosphorylation of unbound
268 GSK3α/β kinase and their inhibition.

269 Furthermore, our expanded analysis of the kinase network and substrate module pattern showed
270 that *AKAP11*-deficiency causes a distortion of PKA, GSK3α/β, and AKT1 activities in neurons
271 (Extended Data Fig. 5b,c). Taken together, our results reveal a fundamental role of AKAP11 in
272 controlling PKA, GSK3a/b, and AKT1 activities in neurons.
273

274 **AKAP11-interactome analysis identifies new partners in PKA-RI adapting and autophagy**
275 **function**

276 To further elucidate AKAP11 function, we investigated the interactome of AKAP11 in CNS
277 neurons. To this end, we generated transgenic mice with Cre-dependent expression of AKAP11-
278 eGFP fusion protein. Crossing the transgenic with Synapsin-Cre mice enabled neuron-specific
279 expression of AKAP11-eGFP fusion in mouse brain (Fig. 5a). Western blotting confirmed the
280 expression of the AKAP11-eGFP fusion protein in the mice with AKAP11-eGFP allele carrying
281 Synapsin-cre (Extended Data Fig. 5d). In addition, AKAP11-eGFP co-localizes with anti-
282 AKAP11 antibody signals in the discrete puncta in neurons (Fig. 5b). Examination of the
283 transgenic showed a wide distribution of the fluorescent AKAP11 fusion in the neurons across
284 mouse brain. AKAP11-eGFP was expressed strongly in the cortex (particularly in layers 2 and

285 5/6), hippocampus (CA3 and DG), and the thalamus, and detected in the pons, and the
286 cerebellum (e.g. Purkinje neuron) (Fig. 5c).

287 We then performed anti-GFP affinity purification, visualized by silver staining (Extended Data
288 Fig. 5e), and conducted mass spectrometry analysis of co-purified proteins with AKAP11. The
289 anti-GFP-bead uncovered over 2000 proteins, of which 59 were significantly enriched compared
290 to the control. As anticipated, we observed significant enrichments of PKA RIα/β (FC 4.08/5.41)
291 (Fig. 5d,e and Supplementary Table 8). The GO terms of the significantly enriched proteins
292 highlight protein kinase A binding and calcium-dependent protein binding (MF), intermediate
293 filament cytoskeleton, extracellular exosome and vesicle, and actin filament (CC), cytoskeleton
294 organization and intermediate filament-based process (BP) (Fig. 5f and Extended Data Fig. 5f).
295 The PPI analysis reveals two distinct clusters, including PKA pathway and calcium signaling,
296 with AKAP11, PKA-RIα/β, SPHKAP, VAPA, and DYRK1A forming an interacting network
297 within PKA cluster, and ANXA1 emerging as the central node in the calcium-dependent protein
298 binding cluster (Fig. 5g). The identification of SPHKAP as a AKAP11-binding protein is
299 intriguing, as SPHKAP protein levels were significantly increased in *AKAP11*-deficient neurons,
300 and it exhibits a strong accordance with PKA subunits within the same protein module (Fig.
301 1b,2h). Moreover, VAP proteins are endoplasmic reticulum (ER)-resident proteins that directly
302 interact with multiple autophagy-related (ATG) proteins. The interaction between ATG proteins
303 and VAPA/B is a prerequisite for autophagosome formation[58,59]. Furthermore, the interaction
304 between VAPA/B and SPHKAP was recently shown to result in the concentration of PKA-RI
305 complex between stacked ER cisternae associated with ER-PM junctions, which is important for
306 the reciprocal regulation of PKA and Ca2+ signaling and the coupling of excitation and
307 transcription[60,61]. Through co-IP experiments we verified the interactions of AKAP11-eGFP with
308 RIα/β, SPHKAP, and VAPA/B (Fig. 5h) in mouse brains with immunoblot analysis.

309 To understand the nature of the interactions between AKAP11, SPHKAP, and VAPA/B in
310 neurons, we next examined their subcellular localization using the transgenic mice expressing
311 AKAP11-eGFP (Extended Data Fig. 6a). Immunofluorescence (IF) imaging showed co-
312 localization of AKAP11-eGFP with the endogenous RIα/β, SPHKAP, and VAPA/B in a fraction
313 of discrete puncta in mouse CNS neurons (Fig. 5i and Extended Data Fig. 6b). Note the low
314 score of the *Pearson*'s coefficient for RIβ, which could reflect the poor specificity of anti-RIβ

315 antibody. Given VAPA/B as ER-residents[62,63] and SPHKAP-VAPA/B complex known for
316 adapting of PKA-RI at the ER-PM junction[61], it raises a possibility that both AKAP11 and PKA-
317 RI are recruited to the ER through interacting with SPHKAP and/or VAPA/B. We also observed a
318 partial co-localization of AKAP11-eGFP with autophagy adaptors p62/SQSTM1 and LC3B in
319 neurons, in agreement with its role in autophagy adapting (Extended Data Fig. 6b).

320 Together, the above findings showed the AKAP11 interactome associated with various cellular
321 pathways. Importantly, the results from the analysis of PKA cluster offer additional support to
322 the function of AKAP11 in regulating PKA protein homeostasis and autophagy process likely
323 through interacting with SPHKAP and VAPA/B adaptor proteins, which are involved in adapting
324 PKA-RI and autophagosome biogenesis[58,60,61].

325

326 **Degradation of PKA adaptor SPHKAP depends on AKAP11-mediated autophagy**

327 We found that the overall staining intensity of SPHKAP protein was markedly enhanced in the
328 cortex and hippocampus of *Akap11*-cKO brains, compared to the control. For instance, a
329 remarkable accumulation of SPHKAP protein was seen in the CA2, CA3, and DG of the
330 hippocampus in *Akap11*-cKO brain (Fig. 6a and Extended Data Fig. 6c). High magnification of
331 IF images showed that the SPHKAP puncta was significantly larger and more abundant in the
332 neurons of *Akap11*-cKO brains than those in control mouse brains (Fig. 6a). Considering the
333 increase of SPHKAP protein levels in *Akap11*-cKO brain (Fig. 1b), the observation suggests that
334 the loss of AKAP11 disrupts the SPHKAP homeostatic levels in neurons.

335 Given the role of AKAP11 as autophagy receptor in PKA-RI degradation[9,10], we next asked if
336 SPHKAP, like PKA-RI, is selectively degraded through autophagy. Examination of our previous
337 proteomics study of *Atg7*-cKO brains (deficient in autophagy)[10] showed a significant enrichment
338 of SPHKAP, RIα/β, and AKAP11 protein levels (but not VAP proteins) (Fig. 6b). Furthermore,
339 SPHKAP protein was accumulated in *Atg7*-cKO neurons with increased number of puncta
340 compared to the control (Fig. 6c). Thus, the evidence from both *Akap11*-cKO (Fig. 1b) and *Atg7*-
341 cKO neurons suggests that AKAP11 mediates selective degradation of SPHKAP through
342 autophagy.

343 To ask if AKAP11 regulates the function of SPHKAP and VAPA/B in adapting PKA-RI at ER,
344 we assessed the subcellular localization of SPHKAP, VAPA/B, and PKA-RI in *Akap11*-cKO
345 brains. Remarkably, IF staining showed that SPHKAP and VAPA were accumulated and
346 colocalized in the large puncta, with a significant increase in both the SPHKAP-VAPA puncta
347 number and size in the neurons of *Akap11*-cKO brains, compared to the control. RIβ exhibited
348 extensive co-localization with SPHKAP-VAPA puncta (Fig. 6d,e,f). The results suggest that the
349 loss of AKAP11 does not disrupt the interactions between SPHKAP, VAP proteins, and RIβ.
350 Instead, lacking AKAP11 resulted in the expansion of the SPHKAP-VAPA-RIβ puncta
351 structures, suggesting an impairment of the clearance. Furthermore, IF staining showed a partial
352 colocalization of p62 signal with the SPHKAP-VAPA puncta, evidenced in the hippocampus
353 from *Akap11*-cKO brain (Fig. 6g). Similar results of the enhanced co-localization for the three
354 proteins were observed in primary neurons from *Akap11*-wKO mice (Extended Data Fig. 6d,e).
355 Taken together, these data suggest that AKAP11 is not required for the function of
356 SPHKAP/VAP proteins in adapting PKA-RI to ER; rather AKAP11 mediates the degradation of
357 SPHKAP alongside PKA-RI through selective autophagy.

358 To evaluate whether AKAP11 regulates VAPA degradation through direct interaction, we
359 generated a mutant AKAP11 lacking a functional FFAT motif, which is known to mediate
360 binding to VAP proteins[60]. Immunoprecipitation (IP) showed that the FFAT-mutant AKAP11
361 failed to interact with VAPA and VAPB, while wild-type AKAP11 exhibited robust binding in
362 transfected HEK293T cells (Fig. 6h). In addition, co-localization between AKAP11 and VAPA
363 was markedly disrupted by the FFAT mutant, as shown by IF imaging in both HEK 293T cells
364 and primary neurons (Fig. 6i,j and Extended Data Fig. 6f). These findings suggest that the FFAT
365 motif is required for the AKAP11-VAPA interaction, potentially enabling the recruitment of the
366 AKAP11 to the ER.

367

368 **Impaired spontaneous neurotransmitter release in *AKAP11*-deficient neuron**

369 To investigate whether *AKAP11*-deficiency affects synaptic function, we performed
370 electrophysiological recordings to measure miniature excitatory postsynaptic currents (mEPSCs)
371 in *AKAP11*-cKO mice under the presence of tetrodotoxin (TTX) and GABAA receptor blocker

372 picrotoxin (PTX). Given the critical role of the PFC in SCZ and BD pathophysiology[64–68], we
373 investigated neuronal transmission in layer 5/6 PFC of *Akap11*-cKO mice (Fig. 7a). Compared to
374 the controls, *Akap11*-cKO neurons exhibited a significant decrease in mEPSC frequency and
375 amplitude (Fig. 7b,c), indicating impaired excitatory synaptic transmission. To further
376 investigate the underlying mechanisms, we also analyzed mEPSC kinetics and found no
377 significant differences in rise time, decay, or half-width between groups (Extended Data Fig. 7a).
378 However, both peak amplitude and area under the curve were significantly decreased in *Akap11*-
379 cKO mice (Fig. 7d), suggesting diminished AMPA receptor-mediated synaptic responses.

380 To test whether the reduced mEPSC frequency was due to a loss of synapses, we performed IF
381 staining in primary neurons. We found a significant reduction in the density of synaptophysin
382 (SYP), PSD95, and co-localized SYP-PSD95 puncta in both *Akap11*-cKO and *Akap11*-wKO
383 neurons compared to the control (Fig. 7e,f and Extended Data Fig. 7b), indicating a reduction in
384 the number of mature excitatory synapse, which could explain the reduced mEPSC frequency.

385 Next, we investigated whether *AKAP11*-KD affects synaptic transmission in human iNeurons.
386 To quantify changes in excitatory synaptic function, we recorded miniature excitatory
387 postsynaptic currents (mEPSCs) under the same condition as in *Akap11*-cKO mice. Our analysis
388 revealed a large decrease (~3 fold) in the frequency of mEPSCs in *AKAP11*-KD human
389 iNeurons, while the amplitude remained unaffected (Fig. 7g-k). Consistent with this, IF staining
390 revealed a decrease in SYP-labeled signal density in *AKAP11*-KD iNeurons (Fig. 7l),
391 phenocopying those in *Akap11*-cKO neurons, indicating disrupted synaptic vesicle protein
392 homeostasis and impaired presynaptic transmission caused by AKAP11 deficiency.

393

394 **Discussion**

395 Our current study reports a comprehensive analysis of autophagy receptor AKAP11's cellular
396 pathways and functions by employing multi-omics approaches, cell biology study, and
397 electrophysiology analysis. Our data delineate a landscape of AKAP11-regulated proteome,
398 kinome, transcriptome, and interactome, which reveals a central role of AKAP11 in coupling the
399 type I PKA complex regulation to synaptic transmission in both human neurons and mouse

models. Our study identifies a novel function of AKAP11 in autophagy by interacting with PKA-RI adaptors SPHKAP and VAPA/B. Given the genetic evidence linking *AKAP11*-coding variants to the shared risk of BD and SCZ[2,3,65], our studies shed a light on the molecular and cellular mechanisms underlying the psychiatric diseases.

Our study demonstrates a pivotal role of AKAP11 in controlling homeostasis and activity of the type I PKA kinase and GSK3α/β in neurons. Multiple lines of evidence from our data reveal that *AKAP11*-deficiency leads to a disruption of homeostasis of PKA activity in neurons. Firstly, the proteomics study of *AKAP11*-KO neurons reveals the increase of regulatory subunits RIα/β and multiple inhibitors of PKA activity, including ADRA2A, PDE4B, PDE3A, and PKIB (Fig. 1b,e and Extended Data Fig. 1b); secondly, phosphoproteomics analysis identifies altered abundancy of predicted PKA phosphorylation sites (Fig. 3c); thirdly, the direct measurement of PKA activity showed a decrease of PKA activity in cytosol but an increase in synaptosome fractions of the brains of *Akap11*-cKO mice (Fig. 3d,e,f). The compartment-specific changes of the PKA activity in *AKAP11*-depleted neurons are not surprising, considering the functions of various AKAP in adapting PKA complex and regulating PKA activity in specific cellular compartments[69]. Interestingly, AKAP11 is highly enriched in cytosol and rarely detectable in synaptosomes fraction (Fig. 3d), consistent with the IF images of AKAP11 localization in the soma (Fig. 5b), whereas PKA-RIα/β and PKA-C are abundantly distributed in both cytosol and synaptosomes (Fig. 3d). The above data suggests the action of AKAP11 occurs primarily in the cytosol or soma, while the loss of AKAP11 impairs the selective autophagic degradation of PKA-RIα/β and PKA-C in the cytosol, resulting in an overflow of PKA-RIα/β and PKA-C proteins in multiple compartments including synaptosomes (Fig. 3d). However, the increase of RIβ is much robust in the cytosol (6.41-fold) than in synaptosome (1.47-fold); in contrast, the PKA-C shows a stronger accumulation in the synaptosome (3.09-fold) than in the cytosolic (1.52-fold) (Fig. 3d,e). The observation explains the differential changes of PKA activity in the cytosol vs. synaptosomes.

Moreover, our data from phosphoproteome and experimental validation demonstrated a role for AKAP11 in regulating GSK3α/β kinase activity, which is also implicated in psychiatric disease[70–72]. AKAP11 directly binds GSK3α/β[5]; given GSK3α/β as substrates of AKT1[5,57,73], the loss of AKAP11 may expose GSK3α/β protein and render the increase of phosphorylation of GSK3α/β by the elevated AKT1 activity (Fig. 4b-e). Therefore, it remains possible that the

430 binding of AKAP11 prevents GSK3α/β from the inhibitory phosphorylation by AKT1,
431 maintaining the active form of GSK3α/β. Interestingly, PKA was also shown to phosphorylate
432 GSK3α/β at the same sites as by AKT1[6,57,74]. While the identification of the exact kinase
433 responsible for GSK3α/β phosphorylation awaits future investigation, our data reveals a novel
434 function and insight for AKAP11 in regulating GSK3α/β kinase activity through their direct
435 binding. Further, our study suggests that AKAP11 level affects kinase activities beyond PKA and
436 GSK3. But the predicted, extensive interactions among PKA, GSK3α/β, and those detected
437 kinases (Fig. 4a and Extended Data Fig. 5b,c) raises a question that the changes of other kinase
438 activities in *AKAP11*-deficient neurons could be a consequence of altered PKA and GSK3α/β
439 activities.

440 Our study shows an important finding that AKAP11 couples the regulation of PKA signaling
441 networks to synaptic transmission. The notion is supported by the evidence that a network
442 module (WGCNA) shows a strong accordance of PKA-RI complex proteins with synaptic
443 proteins, which are co-regulated by AKAP11(Fig. 2b,c,d,h). In *Akap11*-cKO neurons, the 399
444 phospho-proteins that are altered and predicted as PKA substrates display a significant
445 enrichment in synaptic proteins (Fig. 3g,h), and the transcriptomics analysis reveals an
446 enrichment of downregulated synapse related genes (Extended Data Fig. 2b,c). Furthermore, the
447 depletion of AKAP11 proteins leads to impaired spontaneous synaptic transmission in both
448 human and mouse neurons (Fig. 7c,d,k), demonstrating that an intact AKAP11 is critical for
449 maintaining proper synaptic function through controlling type I PKA kinase and GSK3α/β
450 activities. While these findings support a role for AKAP11 in regulating synaptic function via
451 PKA, the mechanistic link between dysregulated PKA activity and synaptic impairment remains
452 to be clarified. Additionally, the altered activities of other kinases such as GSK3α/β and AKT1
453 observed in AKAP11-deficient neurons may also contribute to synaptic dysfunction, providing a
454 valuable direction for future investigation.

455 Through AKAP11-interactome analysis we uncovered the interactions between AKAP11and
456 SPHKAP as well as VAP proteins in neurons. SPHKAP interacts with RIα/β and plays a role in
457 adapting type I PKA to ER-PM junction through binding VAP proteins, which are ER-resident
458 proteins[62,75,76] and important for autophagosome biogenesis[58,59,77]. The interaction and
459 colocalization of AKAP11 with VAP proteins therefore suggest the recruitment of AKAP11 to

460 ER through VAP, which is involved in autophagosome biogenesis [59,62,77]. Our study shows that
461 AKAP11 is not required for the function of SPHKAP/VAP proteins in adapting PKA-RI to ER,
462 but instead mediates SPHKAP degradation through autophagy, coinciding with the autophagic
463 degradation of RIα/β (Fig. 6a,d,e,f). Together, our study provides an insight of AKAP11-
464 mediated degradation of PKA-RI complex through autophagy and supports a model where
465 AKAP11-SPHKAP interaction co-adapt PKA-RI complex to ER for degradation, while
466 AKAP11-VAP interaction facilitates autophagosome biogenesis by recruiting ATG proteins to
467 ER[58,59]. Thus, the AKAP11-SPHKAP-VAP complex offers an assembly platform to adapt type I
468 PKA complex and recruit autophagy machinery at ER or ER-PM junction, leading to the
469 selective degradation of PKA-RI complex. Such a coordinated action enables a precision control
470 of PKA network homeostasis and compartmental activity coupled with calcium signaling, which
471 dictates the synaptic transmission in neurons (Fig. 8a) [60,61].

472 Although both mouse and human iPSC neuron models showed reduced mEPSC frequency
473 following AKAP11 loss, only the mouse model exhibited decreased amplitude. This suggests that
474 AKAP11-deficiency impairs presynaptic function or synapse number in human iNeurons, rather
475 than postsynaptic strength. The differences may reflect species- or model-specific factors such as
476 neuronal maturity, synaptic structure, or compensatory mechanisms. While our current study
477 focuses on excitatory neurons, the potential contribution of inhibitory neurons to AKAP11-
478 related phenotype remains an important and open question. Future studies will be necessary to
479 investigate whether AKAP11 loss also impacts inhibitory synaptic function.

480 Finally, the DisGeNET annotation of the proteomics and phosphoproteomics data from *Akap11*-
481 cKO neurons demonstrate a remarkable enrichment of psychiatric diseases including SCZ (top
482 ranked), BD, and other mental disorders (Fig. 1i,3b). Given the link of protein-truncating
483 variants of AKAP11 to the significant risk of SCZ and BD, the current characterization of the
484 loss-of-function in autophagy receptor AKAP11 thus shed a light on a shared molecular
485 mechanism underlying both SCZ and BD.

486

487 **Methods**

488 **Animal models**

All animal experiments were approved by the Institutional Animal Care and Use Committee (IACUC) of the Icahn School of Medicine at Mount Sinai and conducted in accordance with relevant ethical guidelines. Mice were housed in social cages under a 12-hour light/dark cycle with ad libitum access to food and water, and their food and water intake were monitored daily.

***Akap11* whole-body knockout (wKO) mice** (B6.Cg-Akap11<tm1.3Jsco/J>, strain #028921, discontinued) were obtained from The Jackson Laboratory. These mice were generated with Floxed exons 6 and 7 in *Akap11* allele. However, the mice suffered germline deletion of exons 6 and 7 without crossing Cre mice for unknown reason. Thus, the mutant mice were used as constitutive KO.

***Akap11* conditional knockout (cKO) mice** were generated with exon 6 flanked by loxP sites. The original mice were first generated using FLP recombinase (C57BL/6N-$A^{tm1Brd}AKAP11^{tm1a(EUCOMM)Hmgu}$/J-Mmucd, Stock number 046552-UCD, MMRRC) to remove the lacZ and Neo cassette, producing floxed ($Akap11^{flox/flox}$) mice. These floxed mice were then crossed with Synapsin-Cre mice to generate *Akap11*-cKO mice, which were used to investigate the neuron-specific functions of *Akap11*.

***Akap11*-eGFP knock-in mice** were generated by fusing *Akap11* with eGFP and inserting it into the ROSA26 locus of B6.129S4-$Gt(ROSA)26^{Sortm2(FLP*)Sor}$/J (strain #012930, Jackson lab) mice using a CRISPR/Cas9-based knock-in (KI) strategy, resulting in the targeted allele. These mice were then crossed with Synapsin-Cre mice to generate AKAP11-eGFP expressing mice for pan-neuronal expression. The strategy is based on the transcript NM_016248.4 and the design for the Cre reporter strains follows Srinivas et al. (2001) (BMC Dev Biol, 1:4). These mice were used to study the expression and localization of Akap11 in neurons.

Primary neuronal culture

Mouse cortices from E16-18 embryos of pregnant females were dissected, and tissues were dissociated by incubating in 0.25% trypsin for 30 minutes at 37°C. The dissociated cells were plated on poly-L-lysin-coated coverslips in cell plates with growth medium composed of B27, Gluta-max, penicillin-streptomycin, and Neurobasal. After 18 days in vitro (DIV18), the cultures were fixed and prepared for immunostaining.

518

519 **Differentiation of iNeuron from human PSCs**

520 Human PSCs were maintained and differentiated into glutamatergic neurons using Ngn2
521 overexpression system. PSCs were dissociated and plated in N2 medium supplemented with 50nM
522 Chroman1, followed by transduction with FUW-TetO-Ngn2-P2A-puromycin and FUW-rtTA
523 lentiviruses. Doxycycline was added to induce Ngn2 expression, and puromycin selection was
524 applied to enrich transduced cells. Neurons were plated with mouse glial cells on Geltrex-coated
525 plates and maintained in Neurobasal A medium with supplements, as previously described[10].
526 Mature neurons were used for experiments 5 weeks after co-culture initiation.

527

528 **Immunocytochemistry**

529 Cells were fixed in 4% paraformaldehyde (PFA) in PBS for 20 minutes at room temperature and
530 then washed three times with PBS. Permeabilization was performed with 0.3% Triton X-100 for
531 15 minutes and blocked with blocking solution (PBS containing 5% goat serum) for 1 hour at room
532 temperature. Primary antibodies, Rabbit anti-AKAP11 (LS-Bio, LS-C374339), Rabbit anti-MAP2
533 (Abcam, ab5392), Sheep anti-RIβ (R&D, AF4177), Mouse anti-SPHKAP[60], Guinea pig anti-
534 Synaptophysin (Synaptic Systems, 101004), Guinea pig anti-p62 (PROGEN, GP62-C), diluted in
535 blocking solution (PBS containing 5% goat serum and 0.2% Triton X-100), with were incubated
536 overnight at 4°C. After washing three times with PBS, secondary antibodies, diluted in PBS, were
537 incubated for 2 hours at room temperature. Images were captured using an LSM 900 confocal
538 microscope, with 10X, 20X, 40X, 63X objectives and the images were processed using ImageJ.

539

540 **Immunohistochemistry**

541 Mouse brains (2-5 months old) were perfused with 4% PFA, fixed overnight, and 30% sucrose for
542 2 days at 4°C. After sucrose removal, the brains were embedded in OCT compounds for
543 cryosectioning and incubated at -80°C. The blocks were transferred to the cryostat 30 minutes
544 before sectioning and incubated. The blocks were cut into 30μm thick sections at -20°C. The
545 sections were placed in the 24-well plate with PBS to remove the OCT compound for 1hour at

546 room temperature. Permeabilization was performed with 0.3% Triton X-100 for 30 minutes and
547 blocked with blocking solution (PBS containing 0.3% Triton X-100 and 10% goat serum) for 1-
548 hour at room temperature. Primary antibodies, Rabbit anti-AKAP11 (LS-Bio, LS-C374339),
549 Rabbit anti-RIα (Cell signaling, 5675S), Sheep anti-RIβ (R&D, AF4177), Mouse anti-SPHKAP[60],
550 Guinea pig anti-Synaptophysin (Synaptic Systems, 101004), Rabbit anti-VAPA (Proteintech,
551 15275-1-AP), Rabbit anti-VAPB (Proteintech, 14477-1-AP), Guinea pig anti-p62 (PROGEN,
552 GP62-C), diluted in blocking solution (PBS containing 5% goat serum and 0.2% Triton X-100),
553 were incubated overnight at 4°C. After washing three times with PBS, secondary antibodies diluted
554 in PBS containing 0.03% Triton X-100, were incubated for 2 hours at room temperature. Images
555 were captured using an LSM 900 confocal microscope, with 10X, 20X, 40X, and 63X objectives
556 using Z-stack and tile scan tools and analyzed with Image J.

557

558 **RNA extraction and Bulk RNA-seq DE analysis**

559 Mouse brains, excluding the olfactory bulb and cerebellum, were transferred into RNase-free
560 RINO tubes (Next Advance, Cat# PILR1-RNA) containing 1ml of RLT buffer from RNeasy Mini
561 Kit (Qiagen). The tissues were homogenized using a Bullet Blender (Next Advance). After a brief
562 centrifugation, the homogenates were diluted with additional RLT buffer. Total RNA was isolated
563 by adding 70% ethanol to the homogenates and following the manufacturer's protocol (RNeasy
564 Mini Kit, Qiagen, Cat# 74016). All the RNA libraries were made and sequenced in Experimental
565 Department in Novogene, USA, Sacramento, CA. Sequencing adapters were removed using
566 Trimmomatic[78] and the resulting reads were aligned to the GRCm39 primary assembly using
567 HISAT2[79]. Gene counts for all samples were aggregated into a count matrix, which was
568 subsequently used as input for DESeq2[80] for statistical analysis. Principal component analysis
569 (PCA) of the normalized, variance-stabilized count matrix revealed no outliers. Log2 fold changes
570 and differential expression analysis were estimated using the DESeq function. A false discovery
571 rate (FDR) threshold of 0.05 was applied to identify significantly differentially expressed genes.

572

573 **Western blot analysis of mouse brain lysate**

574 After perfusion with PBS, whole brains were collected from mice, and the olfactory bulb and
575 cerebellum were removed. The remaining brain tissue was homogenized using a Dounce
576 homogenizer in lysis buffer containing 50mM Tris-HCl, pH 7.5, 150mM NaCl, 1% Triton X-100,
577 and proteinase/phosphatase inhibitor. The homogenate was incubated on ice for 30 minutes and
578 centrifuged at 1,200 x g for 10 minutes at 4°C. The supernatant was transferred to a new tube and
579 centrifuged again at 15,000 x g for 20 minutes at 4°C. The final supernatant was collected on ice,
580 and protein concentrations were measured by the Pierce BCA Protein Assay Kit following the
581 manufacturer's protocol.

582 Equal amounts of total proteins were loaded on 4%-12% Bis-Tris gel for SDS-PAGE and
583 transferred to a 0.45μm PVDF membrane. Membranes were blocked in LI-COR Blocking Buffer
584 (LI-COR, 927-60001) for 1 hour at room temperature. Primary antibodies, Rabbit anti-AKAP11
585 (LS-Bio, LS-C374339), Rabbit anti-RIα (Cell signaling, 5675S), Sheep anti-RIβ (R&D, AF4177),
586 Mouse anti-RIIα (BD, 612242), Rabbit anti-PKACα (Cell signaling, 4782S), Rabbit anti-p-
587 PKACα^{T197} (Cell signaling, 5661S), Mouse anti-β-actin (Cell signaling, 3700S), Rabbit anti-
588 ADRA2A (Proteintech, 14266-1-AP), Rabbit anti-SPHKAP (Thermo, PA5-27581), Rabbit anti-
589 Synaptophysin (Thermo, MA5-14532), Rabbit anti-GSK3α/β (Cell signaling, 5676S), Rabbit anti-
590 p-GSK3α/β (S21/S9) (Cell signaling, 9331S), Rabbit anti-p-GluA1^{S845} (Cell signaling, 8084),
591 Rabbit anti-GluA1 (Cell signaling, 13185), Rabbit anti-Akt1 (Cell signaling, 4691S), Rabbit anti-
592 p-Akt1^{S473} (Cell signaling, 4060S), Chicken anti-GFP (Invitrogen, A10262), Rabbit anti-VAPA
593 (Proteintech, 15275-1-AP), Rabbit anti-VAPB (Proteintech, 14477-1-AP), Guinea pig anti-p62
594 (PROGEN, GP62-C), Rabbit anti-LC3A/B (Cell signaling, 12742S), were diluted in blocking
595 buffer with 0.2% Tween-20 and incubated overnight at 4°C. Secondary antibodies were diluted in
596 blocking buffer with 0.2% Tween-20 and 0.01% SDS, followed by a 1-hour incubation at room
597 temperature. Membranes were imaged using LI-COR imaging system and processed with ImageJ
598 software.

599

600 **Immunoprecipitation**

601 Brain tissue, excluding the olfactory bulb and cerebellum, was homogenized in sucrose buffer
602 containing 250mM sucrose, 20mM Tris-HCl (pH 7.5), 0.5mM MgCl2, 0.5mM CaCl2, and

603 protease/phosphatase inhibitors using a Dounce homogenizer. The homogenate was centrifuged at
604 1,000 x g for 10 minutes at 4°C. The supernatant was transfer to a prechilled tube and an equal
605 volume of 2X RIPA buffer (40mM Tris-HCl, pH 7.5, 300mM NaCl, 2% NP-40, 1% sodium
606 deoxycholate, and protease/phosphatase inhibitors) was added. The mixture was incubated at 4°C
607 for 1 hour with rotation and then centrifuged at 15,000 x g for 20 minutes at 4°C. The supernatant
608 was collected, and an aliquot was reserved as input.

609 For GFP-immunoprecipitation, 1mg of protein lysate was incubated overnight at 4°C with GFP-
610 trap® magnetic particles (Chromotek, Cat# gtdk) under rotation. Beads were washed with RIPA
611 buffer and bound proteins were eluted using 50µl of 1X SDS buffer by heat shock at 70°C for 10
612 minutes, repeated twice. The eluted proteins were subjected to SDS-PAGE. Subsequent steps
613 followed the Western blot protocol described above.

614 For HA-immunoprecipitation, 500µg of protein lysates were incubated overnight at 4°C with anti-
615 HA antibody (Santa Cruz, sc-7392) and anti-IgG antibody (Santa Cruz, sc-2025) under rotation.
616 The next day, the lysates were incubated with Dynabeads™ Protein G (Thermo, 10003D) for 2
617 hours at 4°C. After washing the beads with RIPA buffer, bound proteins were eluted with 30µl of
618 2X SDS sample buffer by heating at 95°C for 5 minutes. The eluted proteins were analyzed by
619 SDS-PAGE followed by western blotting as described above.

620

621 **Purification of synaptic fractions**

622 Synaptic fractions were isolated following a previously established protocol[81]. Briefly, mice brains
623 were mechanically homogenized on ice using glass homogenizer (20 slow strokes) in a
624 homogenization buffer containing 5mM HEPES (pH 7.4), 1mM $MaCl_2$, 0.5mM $CaCl_2$, and
625 protease and phosphatase inhibitors. The homogenate was first centrifuged at 1,400 g for 10 min
626 at 4°C, and the resulting supernatant was further centrifuged at 13,800 g for 10 min at 4°C to obtain
627 the pellet. The resulting supernatant was collected as the cytosolic fraction. The pellet was
628 resuspended in 0.32M sucrose, 6mM Tris-HCl (pH 7.5) and carefully layered onto a discontinuous
629 sucrose gradient (0.85M, 1M, and 1.2M sucrose, all in 6mM Tris-HCl, pH 7.5). Ultracentrifugation
630 was performed at 82,500 g for 2 hours at 4°C, and the synaptic fraction, located at the interface
631 between the 1M and 1.2M sucrose layers, was collected. To extract synaptic proteins, the collected

632 synapse was mixed with an equal volume of 1% Triton X-100 (in 6mM Tris-HCl, pH 7.5),
633 incubated on ice for 15min, and centrifuged at 32,800 g for 20 min at 4°C. The final pellet,
634 representing the synaptic fraction, was resuspended in lysis buffer for downstream analysis.

635

636 **Measurement of PKA activity**

637 To measure PKA activity, perfusion with PBS was performed prior to tissue collection. Brain
638 lysates from *Akap11*-cKO mice (excluding the olfactory bulb and cerebellum) and
639 cortex/hippocampus lysates from *Akap11*-wKO mice were analyzed using the PKA activity kit
640 (EIAPKA, Invitrogen) according to the manufacturer's instructions.

641 Briefly, PKA standards or diluted samples, along with reconstituted ATP, were added to a PKA
642 substrate-coated 96-well plate. The plate was incubated at 30°C for 90 minutes while shaking.
643 After incubation, a Donkey anti-Rabbit IgG HRP-conjugated antibody was added, followed by
644 the phospho-PKA substrate antibody, as per the protocol. The plate was incubated at room
645 temperature while shaking for 60 minutes. TMB substrate was then added, and the reaction
646 proceeded for 30 minutes at room temperature. Finally, stop solution was added, and the
647 absorbance at 450nm was measured using a microplate reader.

648

649 **Protein extraction and digestion for mouse brain and iNeurons**

650 Proteins in the tissues of mouse brains or iPSC cells were extracted into the lysis buffer by beads
651 beating in a Bullet Blender at a speed of 6 for 30 s with an interval of 10s at 4^0C for 6 cycles.
652 The lysis buffer contained 8 M urea, 0.5% sodium deoxycholate, phosphatase inhibitor cocktails
653 (Roche) and 50 mM HEPES pH 8.5. The proteins were digested with LysC (200:1 protein:
654 enzyme ratio by weight, Wako) in the presence of 10 mM DTT and 5% acetonitrile for 3 h,
655 followed by a 4-fold dilution with 50 mM HEPES buffer pH 8.5 and overnight trypsin digestion
656 (50:1 protein : enzyme by weight, Promega) at room temperature. The peptides were desalted on
657 C18 SPE column and dried under vacuum.

658

659 **Phosphopeptides enrichment of *Akap11*-cKO mouse brain samples**

660 The phosphopeptides enrichment was carried out on TiO2 beads as previously described[82].
661 Briefly, ~ 300 µg peptides were dissolved in 30 µL of binding buffer (65% acetonitrile, 2% TFA,
662 and 1 mM KH2PO4). TiO2 beads (~1 mg) were washed twice with washing buffer (65%
663 acetonitrile, 0.1% TFA), mixed with the peptide solution, and incubated with end-over-end
664 rotation at room temperature for 20 min. The phosphopeptide-bound beads were collected by
665 brief centrifugation, washed twice with 200 µL washing buffer, and transferred to a C18
666 StageTip (Thermo Fisher Scientific). The phosphopeptides were eluted from StageTip with
667 elution buffer (15 µL, 15% NH_4OH, 40% acetonitrile). The eluents were dried under vacuum and
668 stored at -80^{0}c before MS analysis.

669

670 **Liquid Chromatography-Tandem Mass Spectrometry (LC-MS/MS) Analysis**

671 For MS analysis, the dried peptides were dissolved in 5% formic acid and separated on a reverse
672 phase column (50 µm × 15 cm, 1.7 µm C18 resin from CoAnn Technology) interfaced with a -
673 timsTOP SCP MS (Bruker Daltonics) using nano-Elute 2 liquid chromatography system.
674 Peptides were eluted at 55 °C by 5−27% buffer B gradient in 45 min (buffer A, 0.1% formic acid
675 in water; buffer B, 0.1%formic acid in acetonitrile, flow rate of 0.25 µL/min). The peptides were
676 ionized by a CaptiveSpray nanoelectrospray ion source, introduced into the MS and analyzed by
677 a diaPASEF approach. The mass range was set as 100−1700 m/z and the ion mobility range was
678 0.70−1.30 1/K0.

679

680 **DIA based protein and phosphopeptides identification and quantification**

681 To detect and quantify peptides and proteins, the raw data were searched by Spectronauts
682 (version 18) against a mouse database that contains 55,260 entries or human database with
683 81,791 entries. Fixed and variable modifications included carbamidomethyl, methionine
684 oxidation and N-termini acetylation. Additional phosphorylation at serine/threonine/tyrosine
685 (S/T/Y) was enabled as variable modification for phosphoproteomic analysis. Both peptide and
686 protein FDRs were controlled under 1%. Differentially expressed proteins/peptides were
687 determined using both FDR and log2 fold change (FC) calculated by the limma[83] R package. The
688 significance of differential expression was evaluated based upon statistical criteria, with FDR <

689 0.05 and Log2(FC) > 2SD, or *P*-value < 0.05 and Log2(FC) > 2SD/1.5SD, followed by FDR
690 estimation through permutation (FDR<0.05). The SD of proteins was estimated by fitting to a
691 Gaussian distribution to evaluate the magnitude of experimental variations.

692

693 **TMT based protein identification and quantification**

694 The TMT based proteomics analysis was performed as described before[84]. Briefly, the digested
695 peptides were resuspended in 50 mM HEPES (pH 8.5) for TMTpro labeling, then were equally
696 mixed and fractionated by offline basic pH reverse phase LC. Each of these fractions was
697 analyzed by the acidic pH reverse phase LC-MS/MS on Q Exactive HF Orbitrap mass
698 spectrometer. For mass spectrometer settings, positive in mode and data-dependent acquisition
699 were applied with one full MS scan followed by a 20 MS/MS scans. MS1 scans were collected at
700 a resolution of 60,000, 1×10^6 AGC and 50 ms maximal ion time; MS2 spectra were acquired at
701 a resolution of 60,000, fixed first mass of 120 m/z, 410–1600 m/z, 1×10^5 AGC, 110ms maximal
702 ion time, and ~15 s of dynamic exclusion. The TMT dataset was processed by the JUMP
703 software suite. The raw files were searched against a mouse database with 59,423 entries
704 downloaded from Swiss-Prot, TrEMBL, and UCSC databases. Main search parameters were set
705 at precursor and product ion mass tolerance (± 15 ppm), full trypticity, maximal modification
706 sites (n = 3), maximal missed cleavage (n = 2), static mass shift including carbamidomethyl
707 modification (+57.02146 on Cys), TMT tags (+304.20714 on Lys and N-termini), and dynamic
708 mass shift for oxidation (+15.99491 on Met). Peptide-spectrum matches (PSM) were filtered by
709 mass accuracy, clustered by precursor ion charge, and the cutoffs of JUMP-based matching
710 scores (J-score and ΔJn) to reduce FDR below 1% for proteins.

711

712 **Weighted Gene Correlation Network Analysis (WGCNA)**

713 The analysis was carried out with the WGCNA[39] R package. For the *Akap11*-cKO mouse brain
714 proteomic data, we used the blockwiseModules function to generate the network, with the
715 settings soft-threshold power = 16, minimum module size = 30, network type = ‘‘signed’’,
716 TOMType = “signed”, randomSeed = 1234, pamRespectsDendro = FALSE, maxBlockSize =
717 20,000, and merge cut height = 0.25. The partitioning around medoids-like (PAM-like) stages of

718 module detection was disabled to ensure that module assignments adhered strictly to the
719 hierarchical clustering dendrogram (pamRespectsDendro = FALSE). The soft-threshold power of
720 16 was chosen based on the fitted signed scale-free topology model (R2) approaching an
721 asymptote of 0.85 at that threshold. Furthermore, the mean connectivity at that power was less
722 than 100. The maximum block size was set at 20,000 to complete all clustering within a single
723 block. To get a more robust result, combined our *Akap11*-cKO mouse brain proteomic dataset
724 with our previous work[10]. While for the *AKAP11*-KD iNeuron proteomic data, the settings were:
725 soft-threshold power = 18, minimum module size = 80, network type = ‘‘signed’’, TOMType =
726 “signed”, randomSeed = 1234, pamRespectsDendro = FALSE, maxBlockSize = 20,000. We also
727 combined our *AKAP11*-KD iNeuron proteomic data with our previous work[10].

728

729 **Protein-Protein Interaction (PPI) Network Analysis**

730 The protein-protein interaction network analysis was performed using the STRING[41] plugin in
731 CytoScape[85], with the fold changes and FDR/*P*-values obtained from the differentially expressed
732 proteins analysis. Briefly, for the Akap11-cKO mouse brain proteomic data in ME15, we
733 analyzed the PPI network among these proteins using STRING. Subsequently, we adjusted the
734 node colors and sizes based on the fold changes and FDR obtained from differentially expressed
735 protein analysis presented in Fig. 1b. We performed a similar analysis with the enriched proteins
736 from the AKAP11 interactome data.

737

738 **Pathway enrichment analysis**

739 GO term and GSEA were performed with the R Bioconductor package clusterProfiler[23]. Briefly,
740 we first transfer the proteins symbols to Entrez IDs based on Bioconductor annotation data
741 package (org.Hs.eg.db/org.Mm.eg.db) and used the clusterProfiler::enrichGO or
742 clusterProfiler::gseGO with the pvalueCutoff = 0.05, qvalueCutoff = 0.05 to do pathway
743 enrichment analysis. For human disease enrichment analysis, we utilized the ToppGene Suite[86] in
744 conjunction with the DisGeNET[38] database to do enrichment analysis and generate the dot plot
745 utilizing the ggplot2[87] package. All the volcano plots were generated by EnhancedVolcano[88] R
746 package.

747

748 **Phosphoproteomic data analysis**

749 The analysis of phosphoproteomic data was generally followed as outlined in the paper
750 introducing PhosR[51], which employs a multi-step framework comprising two major components:
751 the first components is the kinaseSubstrateScore function, which evaluates a given phosphosite
752 by integrating kinase recognition motifs and phosphoproteomic dynamics, and the second
753 component is the kinaseSubstratePred function, which combines the scores from the first
754 component for predicting kinase-substrate relationships using an adaptive sampling-based
755 positive-unlabeled learning method[89]. Briefly, we first did the PCA analysis and deleted the
756 outlier one sample in each group (3 Control vs. 3 *Akap11*_cKO) and modified the format of our
757 phosphoproteomic data to conform to the input requirements for PhosR[51,53]. The general analysis
758 workflow comprises the following steps: log transformation, imputation, differentially abundant
759 phosphoprotein site analysis, identifying stably phosphorylated sites, normalization and batch
760 correction of datasets, predicting kinase substrates, and constructing signaling networks
761 (signalomes).

762

763 **Slice Electrophysiology**

764 Electrophysiological recordings from acute prefrontal slices were performed essentially as
765 described previously[90]. Briefly, slices were prepared from *Akap11*-cKO mice aged 2–3 months.
766 Coronal brain slices (300µm thickness) were cut in a high-sucrose cutting solution containing (in
767 mM): 85 NaCl, 75 sucrose, 2.5 KCl, 1.3 NaH_2PO_4, 24 $NaHCO_3$, 0.5 $CaCl_2$, 4 $MgCl_2$, and 25 D-
768 glucose. Slices were equilibrated in artificial cerebrospinal fluid (ACSF) at 31 °C for 30 minutes,
769 followed by an additional hour at room temperature. Slices were then transferred to a recording
770 chamber containing ACSF with the following composition (in mM): 120 NaCl, 2.5 KCl, 1
771 NaH_2PO_4, 26.2 $NaHCO_3$, 2.5 $CaCl_2$, 1.3 $MgSO_4 \cdot 7H_2O$, and 11 D-glucose (~290 mOsm),
772 supplemented with 50 µM picrotoxin and 0.5 µM TTX. Miniature excitatory postsynaptic
773 currents (mEPSCs) from Layer 5–6 cells in the medial prefrontal cortex (mPFC) were recorded
774 in whole-cell voltage-clamp mode (holding potential = -70 mV) using an internal solution with
775 the following composition (in mM): 117 Cs-methanesulfonate, 15 CsCl, 8 NaCl, 10 TEA-Cl, 0.2
776 EGTA, 4 Na_2-ATP, 0.3 Na_2-GTP, and 10 HEPES, pH 7.3 adjusted with CsOH (~300 mOsm). All

recordings were acquired using Clampex 10 data acquisition software (Molecular Devices) and a Multiclamp 700B amplifier (Molecular Devices). Miniature events were manually identified using a 5pA threshold in the Clampfit software.

Patch Clamp electrophysiology in human iN cells

Whole-cell patch-clamp electrophysiology for iNeurons cells was performed as described[91]. To examine intrinsic membrane properties and record action potentials, K-gluconate internal solution (in mM): 126 K-gluconate, 4 KCl, 10 HEPES, 0.05 EGTA, 4 ATP-magnesium, 0.3 GTP-sodium, and 10 phosphocreatine was used. Miniature postsynaptic currents were recorded at a holding potential of −70 mV in the presence of 1 μM tetrodotoxin (TTX) and 50 μM Picrotoxin (PTX). The Cs-based internal solution used for this purpose contained the following components (in mM): 40 CsCl, 3.5 KCl, 10 HEPES, 0.05 EGTA, 90 K-gluconate, 1.8 NaCl, 1.7 $MgCl_2$, 2 ATP-magnesium, 0.4 GTP-sodium, and 10 phosphocreatine.

The external solution used during recordings consisted of (in mM): 140 NaCl, 5 KCl, 10 HEPES, 2 $CaCl_2$, 2 $MgCl_2$, and 10 Glucose, with a pH of 7.4. All recordings of cell culture experiments were performed at room temperature.

To ensure data quality, any cells exhibiting a change in series resistance (Rs) exceeding 20% during the recording were excluded from the analysis. Additionally, recordings with an access resistance greater than 25 MΩ were also excluded. The electrophysiological data were collected using pClamp 10.5 software (Molecular Devices) and the MultiClamp 700B amplifier (Molecular Devices). The detection of miniature excitatory postsynaptic currents (mEPSCs) was performed using the template search algorithm in Clampfit 10.5 software (Molecular Devices).

Quantification and Statistical Analysis

Unless otherwise specified, all data are presented as the means of at least three biological replicates, each derived from a minimum of three independent experiments. Statistical significance between two groups was evaluated using an unpaired, two-tailed Student's t-test. For comparisons involving multiple means, statistical significance was assessed using one-way

analysis of variance (ANOVA) followed by Dunnett's multiple comparisons test, conducted in GraphPad Prism (version 10.2.3; GraphPad Software, CA, USA). Data are reported as mean ± SEM, with specific details regarding statistical tests provided in the respective figure legends. Error bars represent the standard deviation of all replicates. Graphs and plots were generated using GraphPad Prism (version 10.2.3) or RStudio (version 2024.09.1).

Data availability

The authors affirm that all supporting data for the study's findings are readily available within the paper and its Supplementary Information files. For further inquiries regarding resources and reagents, please contact the lead contact, Zhenyu Yue (zhenyu.yue@mssm.edu), Nan Yang (nan.yang1@mssm.edu), Junmin Peng (junmin.peng@stjude.org), and Jinye Dai (jinye.dai@mssm.edu). The source data accompanying this publication are also provided.

Acknowledgements

We are grateful to Dr. Vierra for kindly providing the SPHKAP antibody. The schematics were created using BioRender. This work was supported by the NIH grants R01NS060123 (Z.Y., N.Y., J.P.), R01NS117590 and R21AG067570 (Z.Y. and N.Y.). Z. Pang's laboratory is supported by R01MH131296, R01MH125528 and RM1MH133065. L.W. was supported by the New Jersey Governor's Council for Medical Research and Treatment of Autism Postdoctoral Fellowship (CAUT24DFP).

Author contributions

Zhenyu Yue conceived the study. You-Kyung Lee performed the sample preparation, immunoblot assay, GFP affinity purification, immunoflueoscence staining with *Akap11*-cKO, *Akap11*-wKO mouse brains, and *AKAP11*-deficiency neurons. Cong Xiao did the data analysis of the proteomic data from *Akap11*-cKO and *Akap11*-wKO mouse brains and *AKAP11*-KD iNeurons, the RNAseq data from *Akap11*-cKO, as well as the phosphoproteomic data from *Akap11*-cKO mouse brains. Xianting Li generated *AKAP11*-deficient mouse models and performed the interactome sample

833 preparation, silver staining and GFP affinity purification using AKAP11-eGFP mouse brains.
834 Xiaoting Zhou and Henry Kim assisted generating and analyzing of proteomics of iNeurons.
835 Zhiping Wu and Meghan G. McReynolds performed the proteomics and phospho-proteomics
836 analysis by MS. Le Wang did the electrophysiology analysis of *AKAP11*-KD iNeurons guided by
837 Zhiping Pang. Jinye Dai did the electrophysiology analysis of *Akap11*-cKO mouse neruons.
838 Junmin Peng guided the proteomics data analysis and data interpretation. Zhenyu Yue, You-Kyung
839 Lee, Cong Xiao, Nan Yang, Junmin Peng drafted the manuscript**.**

Figures

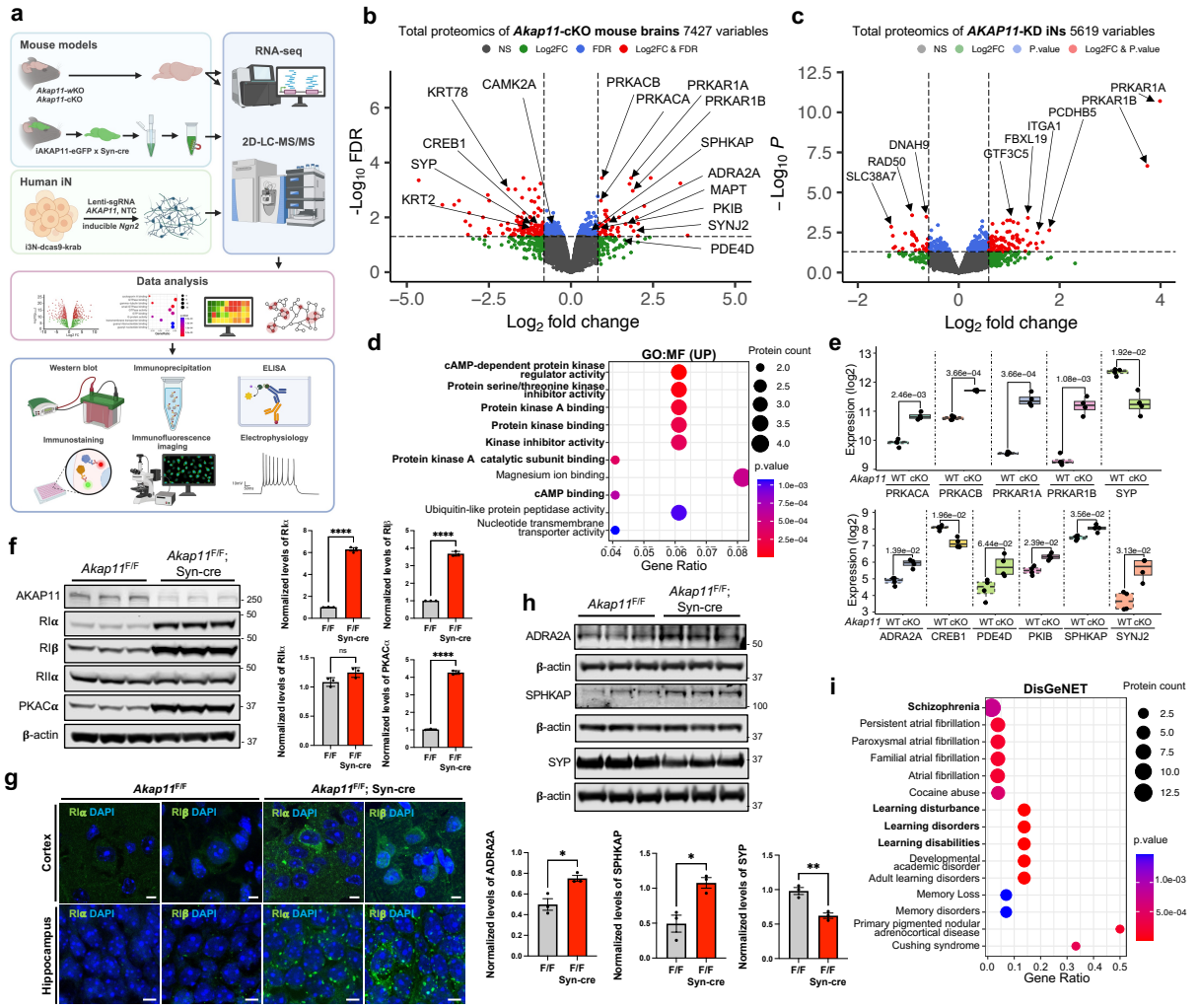

Fig. 1: Integrated proteomic analysis of brain lysate from *Akap11*-cKO mouse brains and *AKAP11*-KD iNeurons.

a, An overview of the study workflow, which integrates multiple-omics, bioinformatics, cell imaging, electrophysiology, and protein biochemistry, and investigates multiple genetic mouse models of AKAP11 and human iNeurons. Created with BioRender.com.

b, Volcano plot of the differentially expressed proteins (DEPs) detected by mass-spectrometry in *Akap11*-cKO mouse brains. A positive score indicates enrichment, a negative score indicates depletion. The y axis represents statistical confidence (adjusted *P*-value (FDR)) for each x axis point. Enriched proteins, defined by FDR < 0.05 and |Log2FC| > 2SD, are colored in red.

c, Volcano plot of the differentially expressed proteins (DEPs) detected by mass-spectrometry in *AKAP11*-KD human iNeurons. A positive score indicates enrichment, a negative score indicates depletion. The y axis represents statistical confidence (*P*-value) for each x axis point. Enriched

854 proteins, defined by *P*-value < 0.05 and |Log2FC| > 2SD and followed by FDR estimation
855 through permutation (FDR<0.05), are colored in red.

856 **d**, Gene Ontology (GO) annotations of the DEPs in **b**, displaying the top 10 enriched pathways
857 with *P*-value < 0.05.

858 **e**, The enrichment levels for the proteins as shown in **b** with log2 transformed DIA intensities
859 across *Akap11*$^{F/F}$ and *Akap11*$^{F/F}$; Syn-cre mice.

860 **f**, Immunoblotting using antibodies against AKAP11 and PKA subunits and quantification of the
861 blot results. Data are presented as mean ± SEM (n=3 per genotype). Statistical analysis was
862 performed using an unpaired *t*-test.

863 **g**, Immunofluorescence (IF) imaging of the cortex and hippocampus from *Akap11*$^{F/F}$ and
864 *Akap11*$^{F/F}$; Syn-cre mice, stained with anti-RIα, anti-RIβ and DAPI. Scale bars, 5μm.

865 **h**, Immunoblotting using antibodies against ADRA2A, SPHKAP, and SYP and quantification of
866 the blot results. Data are presented as mean ± SEM (n=3 per genotype). Statistical analysis was
867 performed using an unpaired *t*-test.

868 **i**, DisGeNet annotations of the DEPs through ToppGene in **b** with *P*-value < 0.05.

869

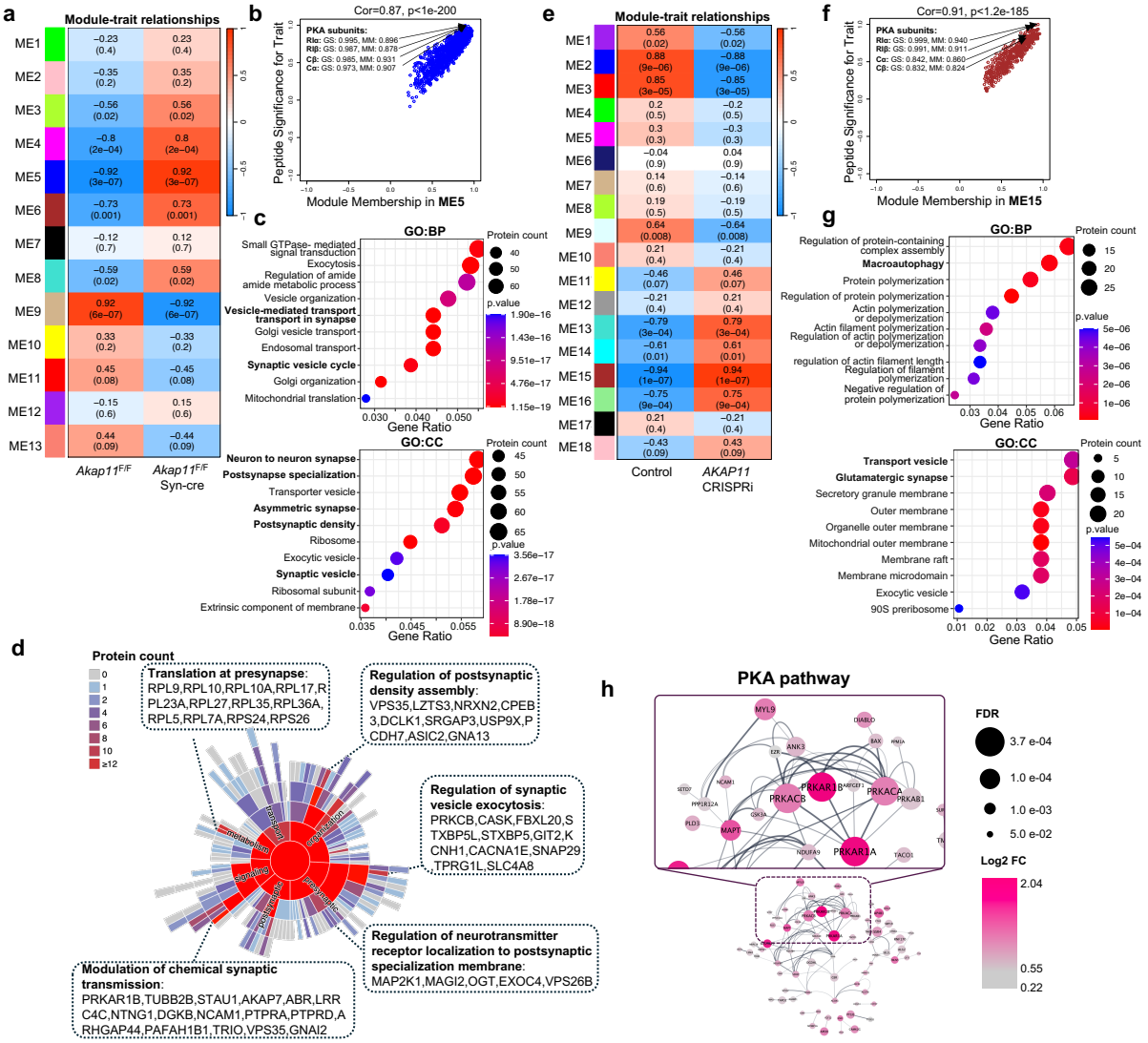

Fig. 2: Identification of co-regulation of cellular pathways upon *AKAP11*-deficiency through WGCNA.

a,**e**, Heatmap of the correlation between the module eigengenes and traits in *Akap11*-cKO mouse brains (16 samples) (**a**) or in *Akap11*-wKO iNeurons (16 samples) (**e**). Red represents positive correlation, and blue represents negative correlation to the trait. The *Pearson* correlation and *P*-value are presented in each module.

b,**f**, Scatter plot of the module membership (x axis) and peptide significance (y axis) in ME5 from *Akap11*-cKO mouse brains (**b**) or ME15 from *AKAP11*-KD iNeurons (**f**).

c,**g** Gene Ontology (GO) annotations of the proteins in ME5 from *Akap11*-cKO mouse brains (**c**) or ME15 from *AKAP11*-KD iNeurons (**g**), displaying the top 10 enriched pathways with *P*-value < 0.05.

883 **d**, Sunburst plots depicting SynGO Biological Process pathways with a *P*-value < 0.05. For
884 selected ontologies, representative proteins from ME5 within the ontology are displayed.

885 **h**, PPI network analysis of proteins in ME5 in **a** (only FDR < 0.05). The color gradience
886 represents from low (grey) to high (red) fold enrichment. Dot size represents statistical
887 significance.

888

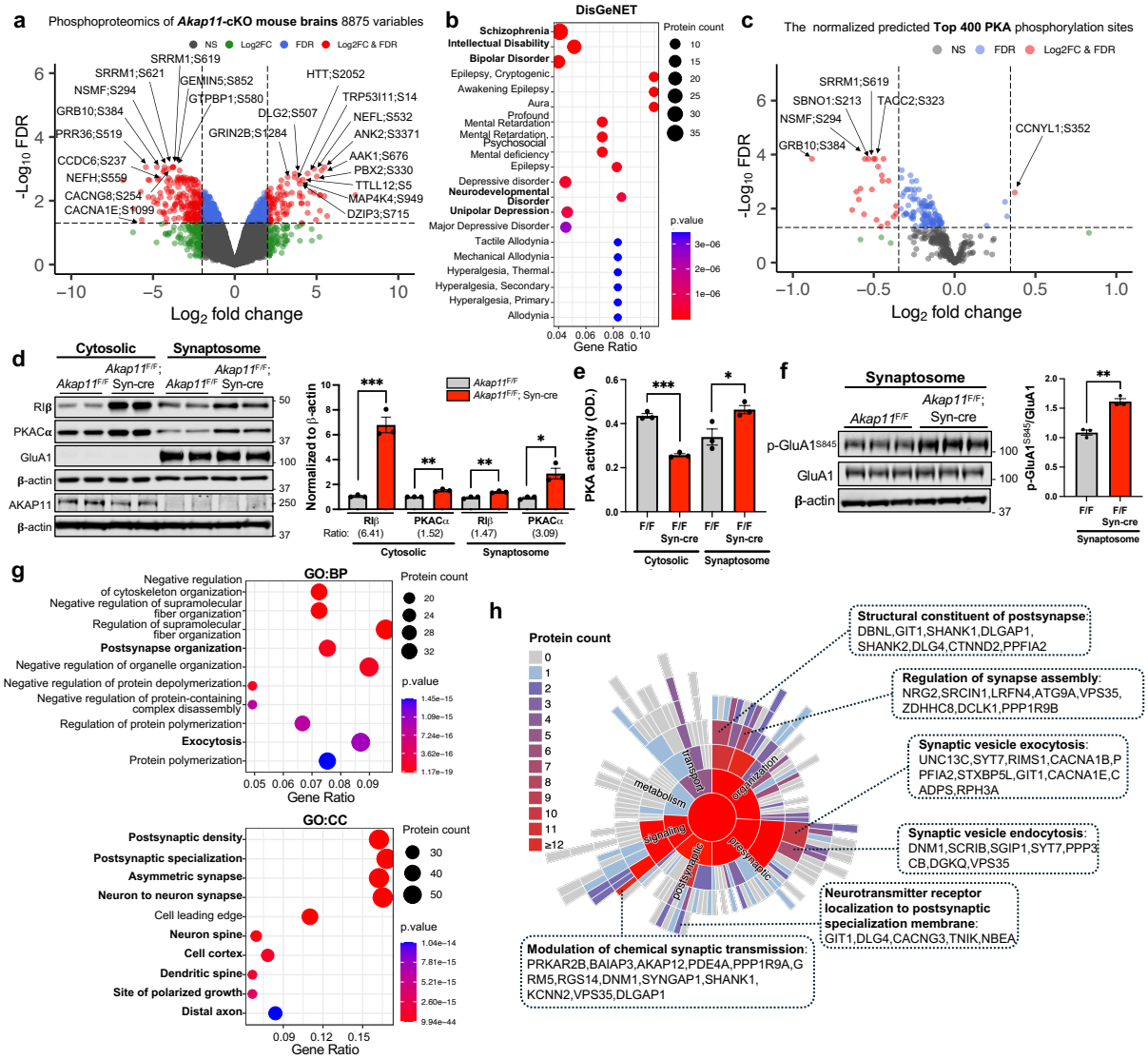

Fig. 3: Phosphoproteomics and PKA activity analysis of *Akap11*-cKO brain lysates.

a, Volcano plot of the differentially abundant phosphoprotein sites (DAPPSs) detected by mass-spectrometry in *Akap11*-cKO mouse brains and *AKAP11*-KD human iNeurons. A positive score indicates enrichment, a negative score indicates depletion. The y axis represents statistical confidence (adjusted *P*-value (FDR)) for each x axis point. Enriched proteins, defined by FDR < 0.05 and |Log2FC| > 2SD, are colored in red.

b, DisGeNet annotations of the DEPPSs through ToppGene in **a** with *P*-value < 0.05.

c, Volcano plot of the top 400 predicted PKA phosphorylation sites (normalized by the total protein level) detected by mass-spectrometry in *Akap11*-cKO mouse brains. A positive score indicates enrichment, a negative score indicates depletion. The y axis represents statistical confidence (adjusted *P*-value (FDR)) for each x axis point. Enriched proteins, defined by FDR < 0.05 and |Log2FC| > 2SD, are colored in red.

902 **d,** Immunoblotting using antibodies against RIβ, PKA-Cα, GluA1, and AKAP11 in cytosolic and
903 synaptosome fractions and quantification of the results. Data are presented as mean ± SEM (n=3
904 per genotype). Statistical analysis was performed using an unpaired *t*-test.

905 **e**, Bar graphs of the ELISA results measuring PKA activity in the cytosol and synaptic fractions
906 from *Akap11*$^{F/F}$ and *Akap11*$^{F/F}$; Syn-cre mice. Data are presented as mean ± SEM. Statistical
907 analysis using an unpaired *t*-test. (n=3 per genotype).

908 **f,** Immunoblotting using antibodies against p-GluA1^{S845} and GluA1 in synaptosome and
909 quantification of the results. Data are presented as mean ± SEM (n=3 per genotype). Statistical
910 analysis was performed using an unpaired *t*-test.

911 **g**, Gene Ontology (GO) annotations of the predicted PKA substrates, displaying the top 10
912 enriched pathways with P-value < 0.05.

913 **h**, Sunburst plots depicting SynGO Biological Process pathways with a P-value < 0.05. For
914 selected ontologies, representative proteins from predicted PKA substrates within the ontology
915 are displayed.

916

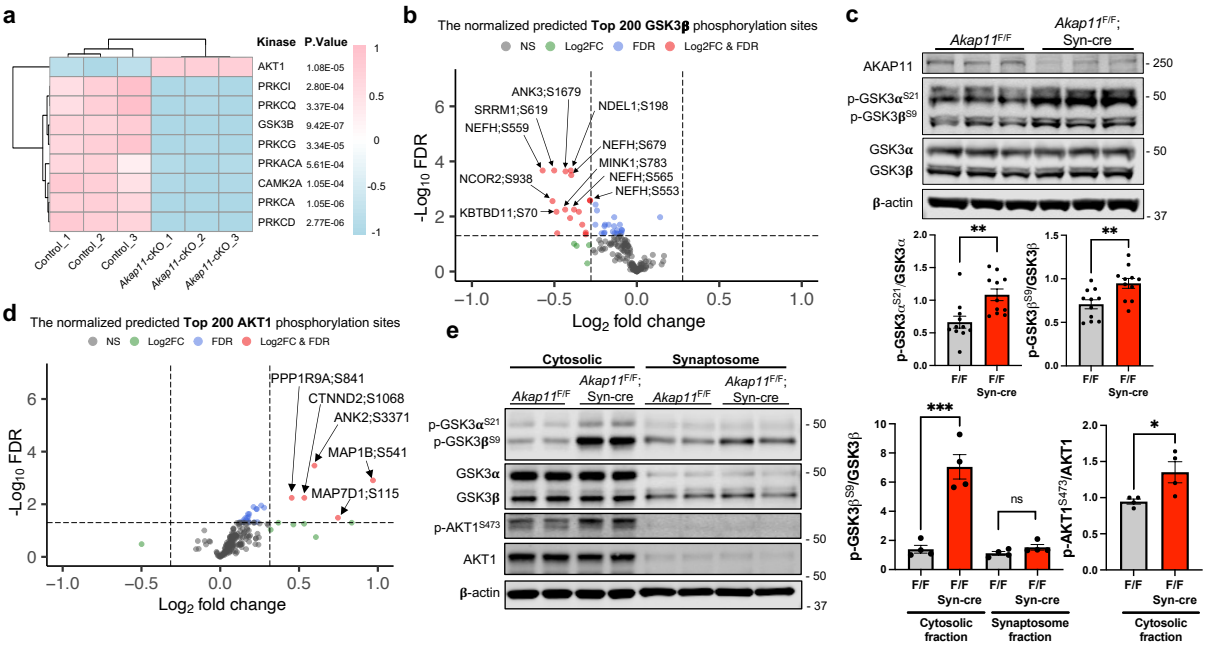

Fig. 4: GSK3α/β kinase activity analysis in *Akap11*-cKO brain lysates.

a, The predicted kinase activity scores for representative kinases. The scores were generated by PhosR based on the phosphorylation levels of predicted substrates. Statistical significance was determined using *t*-test.

b, Volcano plot of the top 200 predicted GSK3β phosphorylation sites (normalized by the total protein level) detected by mass-spectrometry in *Akap11*-cKO mouse brains. A positive score indicates enrichment, a negative score indicates depletion. The y axis represents statistical confidence (adjusted *P*-value (FDR)) for each x axis point. Enriched proteins, defined by FDR < 0.05 and |Log2FC| > 2SD, are colored in red.

c, Immunoblotting using antibodies against AKAP11, GSK3α/β and p-GSK3α/β (S21/S9) and quantification of the results. Data are presented as mean ± SEM (n=11 per genotype). Statistical analysis was performed using an unpaired *t*-test.

d, Volcano plot of the top 200 predicted AKT1 phosphorylation sites (normalized by the total protein level) detected by mass-spectrometry in *Akap11*-cKO mouse brains. A positive score indicates enrichment, a negative score indicates depletion. The y axis represents statistical confidence (adjusted *P*-value (FDR)) for each x axis point. Enriched proteins, defined by FDR < 0.05 and |Log2FC| > 2SD, are colored in red.

e, Immunoblotting using antibodies against p-GSK3α/β (S21/S9), GSK3α/β, p-Akt1^{S473}, and Akt1 in cytosolic and synaptosome fractions and quantification of the results. Data are presented as mean ± SEM (n=4 per genotype). Statistical analysis was performed using an unpaired *t*-test.

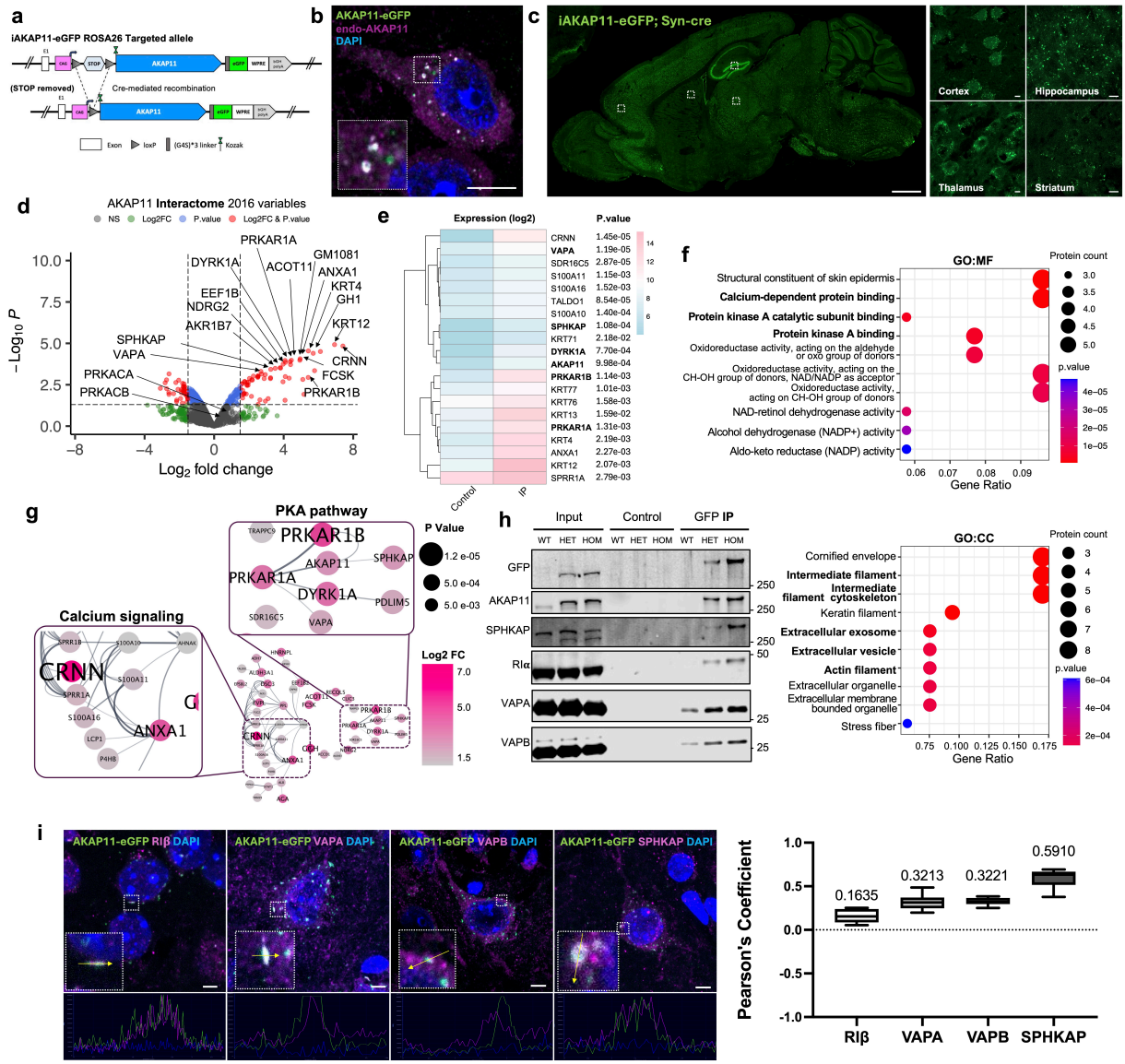

Fig. 5: Characterization of AKAP11 interactome in mouse CNS neurons.

a, Schematic illustration of the generation of AKAP11-eGFP; Syn-cre mice producing the fusion protein in CNS neurons.

b, IF images of AKAP11-eGFP; Syn-cre brain slices stained with anti-GFP (green), anti-AKAP11 antibodies (magenta), and DAPI. Scale bar, 5µm.

c, IF images of sagittal sections from AKAP11-eGFP; Syn-cre mouse brains, showing AKAP11 expression in various brain regions. Inset images provide magnified views of cortex, hippocampus, thalamus, and striatum. Scale bars, 1000µm (main images); 5µm (inset images).

d, Volcano plot of the co-Immunoprecipitated (IP) proteins detected by mass-spectrometry in AKAP11-eGFP mouse brain lysates. A positive score indicates enrichment, a negative score

949 indicates depletion. The y axis represents statistical confidence (*P*-value) for each x axis point.
950 Enriched proteins, defined by *P*-value < 0.05 and |Log2FC| > 1.5SD and followed by FDR
951 estimation through permutation (FDR<0.05), are colored in red.

952 **e**, Enrichment levels of the specific proteins in **d** with log2 transformed DIA intensities across
953 control and AKAP11-eGFP groups.

954 **f**, Gene Ontology (GO) annotations of the proteins shown in **d**, displaying the top 10 enriched
955 pathways with *P*-value < 0.05.

956 **g**, PPI network analysis of proteins shown in **d**. The color gradience represents from low (grey)
957 to high (red) fold enrichment. Dot size represents statistical significance.

958 **h**, IP was performed using Chromotek GFP-trap® particle from heterozygous and homogenous
959 of AKAP11-eGFP transgenic mice and non-transgenic mouse brains and immunoblotting with
960 antibodies against GFP, AKAP11, SPHKAP, RIα, VAPA, and VAPB.

961 **i,** Representative IF images of AKAP11-eGFP mouse brain slices stained with anti-RIβ, anti-
962 VAPA, anti-VAPB, and anti-SPHKAP antibodies in the cortex, showing co-localization of these
963 proteins. Scale bars, 5μm. Co-localization of AKAP11-eGFP with RIβ, VAPA, VAPB, and
964 SPHKAP quantified using Pearson's correlation coefficient calculated with the JACoP plugin.
965 Data are presented as mean ± SEM (n >8 per group).

966

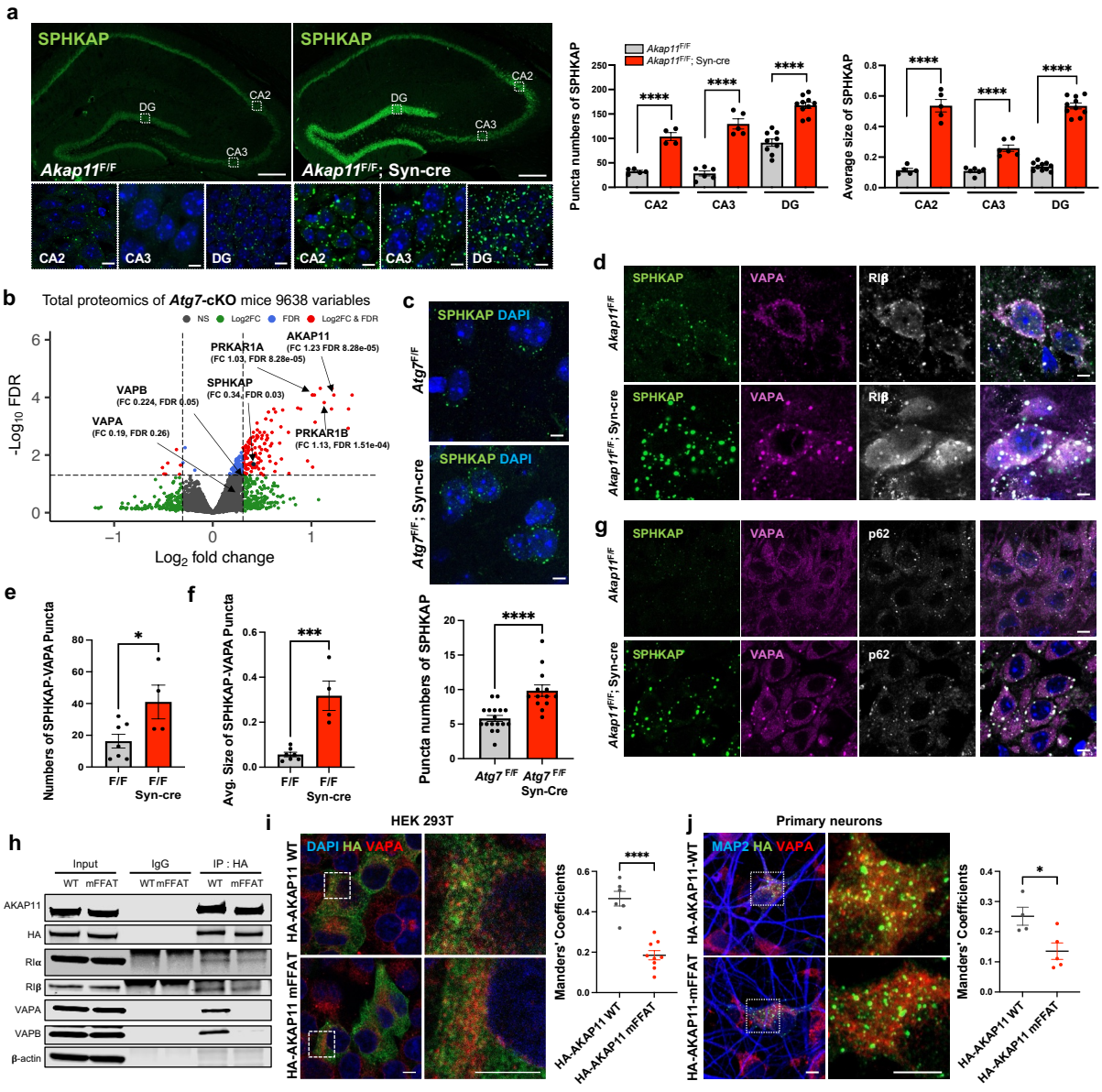

Fig. 6: Characterization of SPHKAP and VAP proteins in neurons from *Akap11*-cKO and *Atg7*-cKO mouse brains.

a, IF imaging of the hippocampal CA2, CA3, and DG of the brains slices from *Akap11*$^{F/F}$ and *Akap11*$^{F/F}$; Syn-cre mice, stained with anti-SPHKAP and DAPI. Inset images provide magnified views of cortex, hippocampus, thalamus, and striatum. Scale bars, 200μm (main images); 5μm (inset images). Bar graph as the quantification of SPHKAP puncta numbers and average size in DAPI-positive cells using Analyze Particles in ImageJ. Data are presented as mean ± SEM (n > 4 per genotype). Statistical significance (****p<0.0001) was performed using an unpaired *t*-test.

b, Volcano plot of the differentially expressed proteins (DEPs) detected by mass-spectrometry in *Atg7*$^{F/F}$ and *Atg7*$^{F/F}$; Syn-cre mouse brains. A positive score indicates enrichment, a negative score indicates depletion. The y axis represents statistical confidence (adjusted *P*-value (FDR))

979 for each x axis point. Enriched proteins, defined by FDR < 0.05 and |Log2FC| > 2SD, are colored
980 in red.

981 **c**, IF imaging of the cortex from *Atg7*$^{F/F}$ and *Atg7*$^{F/F}$; Syn-cre mice, stained with anti-SPHKAP
982 and DAPI. Scale bars, 5 μm. Bar graph as the quantification of SPHKAP puncta numbers per
983 DAPI-positive cell using Analyze Particles in ImageJ. Data are presented as mean ± SEM (n >
984 13 per genotype). Statistical significance (****p<0.0001) was performed using an unpaired *t*-
985 test.

986 **d,e,f,** IF imaging of the cortex from *Akap11*$^{F/F}$ and *Akap11*$^{F/F}$; Syn-cre mice, stained with anti-
987 SPHKAP, anti-VAPA, anti-RIβ, and DAPI. Scale bars, 5 μm. Bar graph as the quantification of
988 SPHKAP-VAPA puncta numbers and average size in DAPI-positive cells using Analyze Particles
989 in ImageJ. Data are presented as mean ± SEM (n >4 per genotype). Statistical significance
990 (*p<0.05 and ***p<0.001) was performed using an unpaired *t*-test.

991 **g**, IF imaging of the cortex from *Akap11*$^{F/F}$ and *Akap11*$^{F/F}$; Syn-cre mice, stained with anti-
992 SPHKAP, anti-VAPA, anti-p62, and DAPI. Scale bars, 5 μm.

993 **h,** Co-immunoprecipitation was performed using anti-HA antibody from HEK293T cells
994 expressing HA-tagged AKAP11 WT or FFAT motif mutant (mFFAT), followed by
995 immunoblotting with antibodies against HA, AKAP11, RIα, RIβ, VAPA, and VAPB.

996 **i,** HEK293T cells expressing HA-AKAP11 WT or mFFAT were stained with antibodies against
997 HA, VAPA, and DAPI. The bar graph shows quantification of HA–VAPA co-localized signal
998 using Manders' coefficient. Data are presented as mean ± SEM (n > 6 per group). Statistical
999 significance (****p<0.0001) was performed using an unpaired *t*-test. Scale bars, 5 μm.

1000 **j,** Primary neurons expressing HA-AKAP11 WT or mFFAT were stained with antibodies against
1001 HA, VAPA, and MAP2. The bar graph shows quantification of HA–VAPA co-localized signal
1002 using Manders' coefficient. Data are presented as mean ± SEM (n > 4 per group). Statistical
1003 significance (*p<0.05) was performed using an unpaired *t*-test. Scale bars, 5 μm.

1004

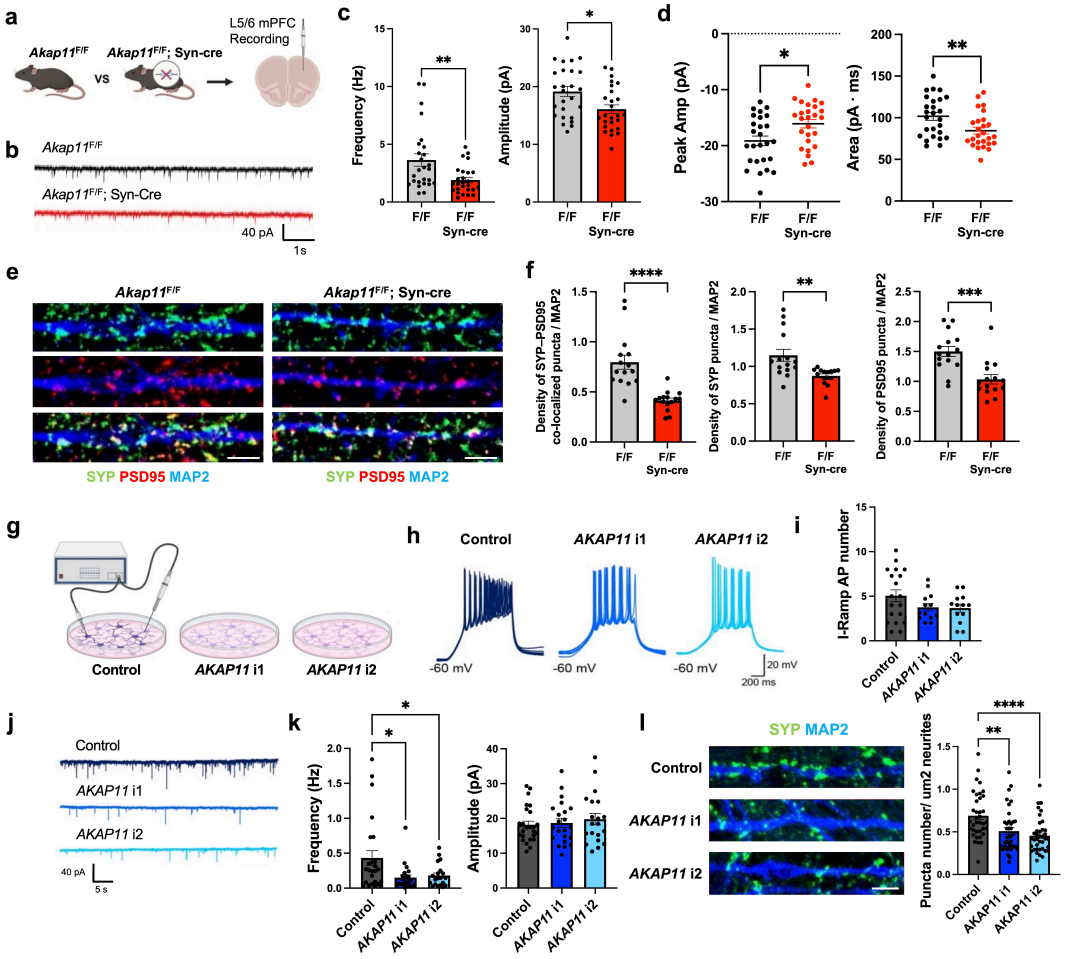

Fig. 7: Electrophysiology analysis of *Akap11*-cKO mouse neurons and human *AKAP11*-KD iNeurons.

a, Schematic images illustrating the electrophysiology experiments in *Akap11*$^{F/F}$ and *Akap11*$^{F/F}$; Syn-cre brain slices.

b, Representative traces of mEPSC in the PFC of *Akap11*$^{F/F}$ and *Akap11*$^{F/F}$; Syn-cre mouse brains.

c, Quantification of mEPSC frequency (left) and amplitude (right) in the PFC of *Akap11*$^{F/F}$ and *Akap11*$^{F/F}$; Syn-cre brain slices. Data are presented as mean ± SEM (n>26 neurons, 3 independent replicates). Statistical significance (*p<0.05 and **p<0.01) was performed using an unpaired *t*-test.

d, Quantification of mEPSC peak amplitude (left) and total charge transfer (area, right) in the PFC of *Akap11*$^{F/F}$ and *Akap11*$^{F/F}$; Syn-cre brain slices. Data are presented as mean ± SEM (n>26 neurons, 3 independent replicates). Statistical significance (*p<0.05 and **p<0.01) was performed using an unpaired *t*-test.

1020 **e,f,** IF imaging of the primary cortical neurons from *Akap11*$^{F/F}$ and *Akap11*$^{F/F}$; Syn-cre mice,
1021 stained with anti-Synaptophysin, anti-PSD95, and anti-MAP2. Scale bars, 5μm. The bar graph
1022 shows quantification of SYP-PSD co-localized puncta, SYP puncta, and PSD95 puncta number
1023 normalized to MAP2. Data are presented as mean ± SEM (n>15 neurons, 3 independent
1024 replicates). Statistical analysis was performed using one-way ANOVA.

1025 **g**, Schematic illustration of the electrophysiology experiments in human *AKAP11*-KD iNeurons.

1026 **h,i,** Representative traces and quantification of induced action potentials (APs) number induced
1027 by a ramp depolarization protocol. Data are shown in mean ± SEM (n>20 neurons, 3
1028 independent replicates).

1029 **j,k**, Representative traces (**h**) and quantification of mEPSC (**i**) (with 1uM TTX and 50uM PTX)
1030 frequency (left) and amplitude (right) in control and two clones of *AKAP11*-KD human
1031 iNeurons. Data are shown in mean ± SEM (n>20 neurons, 3 independent replicates). Statistical
1032 significance (*p<0.05) was evaluated with one-way ANOVA.

1033 **l**, IF imaging and quantification of the *AKAP11*-KD or Control iNeurons, stained with anti-
1034 Synaptophysin and anti-MAP2. Scale bars, 2μm. The bar graph shows quantification of puncta
1035 number per MAP2-positive neurite. Data are presented as mean ± SEM, (n > 37 per genotype).
1036 Statistical analysis was performed using one-way ANOVA.

1037

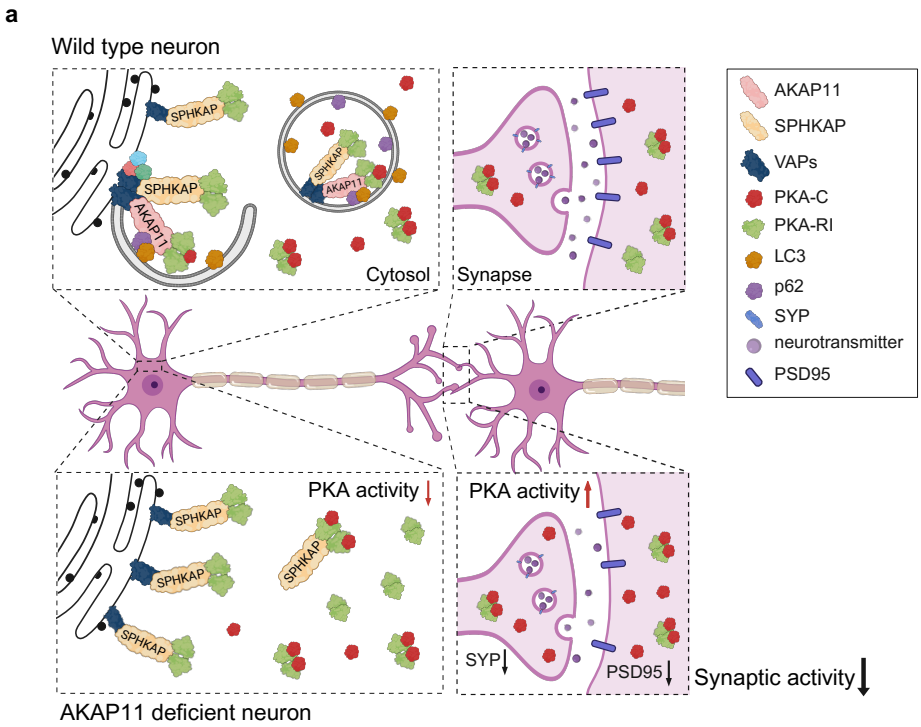

Fig. 8: Graphical summary of AKAP11-regulated PKA signaling and synaptic function.

a, In WT neurons, AKAP11 interacts with SPHKAP and VAPs at the ER to facilitate autophagic degradation of the PKA-RI complex, thereby maintaining compartment-specific PKA activity and normal expression of synaptic markers such as SYP and PSD95. In AKAP11-deficient neurons, impaired degradation leads to accumulation of PKA-RI and PKA-C, resulting in reduced cytosolic and increased synaptic PKA activity. This dysregulation is associated with decreased synaptic marker levels and impaired synaptic activity, highlighting AKAP11's role in compartment-specific PKA regulation and synaptic function.

Supplementary Figures:

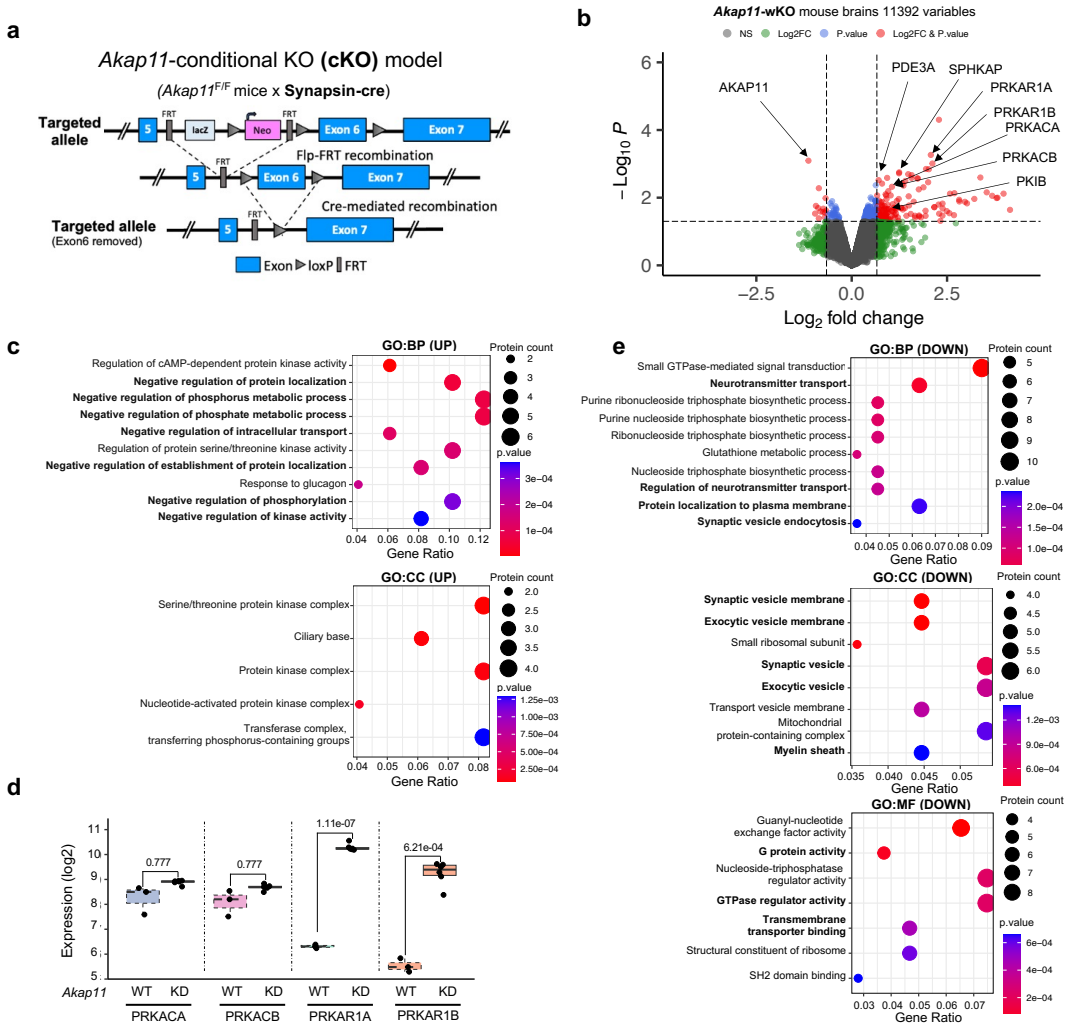

Extended Data Fig. 1: Intergrated proteomics analysis of *Akap11*-cKO and *Akap11*-wKO mouse brains, and *AKAP11*-KD human iNeurons.

a, The strategy for generating the *AKAP11*-cKO mouse model.

b, Volcano plot of the differentially expressed proteins (DEPs) in *Akap11*-wKO mouse brains. A positive score indicates enrichment, a negative score indicates depletion. The y axis represents statistical confidence (*P*-value) for each x axis point. Enriched proteins, defined by *P*-value < 0.05 and |Log2FC| > 2SD and followed by FDR estimation through permutation (FDR<0.05), are colored in red.

c,**e**, Gene Ontology (GO) annotations of the DEPs in **Fig. 1b**, displaying the top 10 enriched pathways with *P*-value < 0.05.

1060 **d**, Enrichment levels for the proteins as shown in **Fig. 1c** with log2 transformed TMT intensities
1061 across AKAP11-eGFP and control mice.

1062

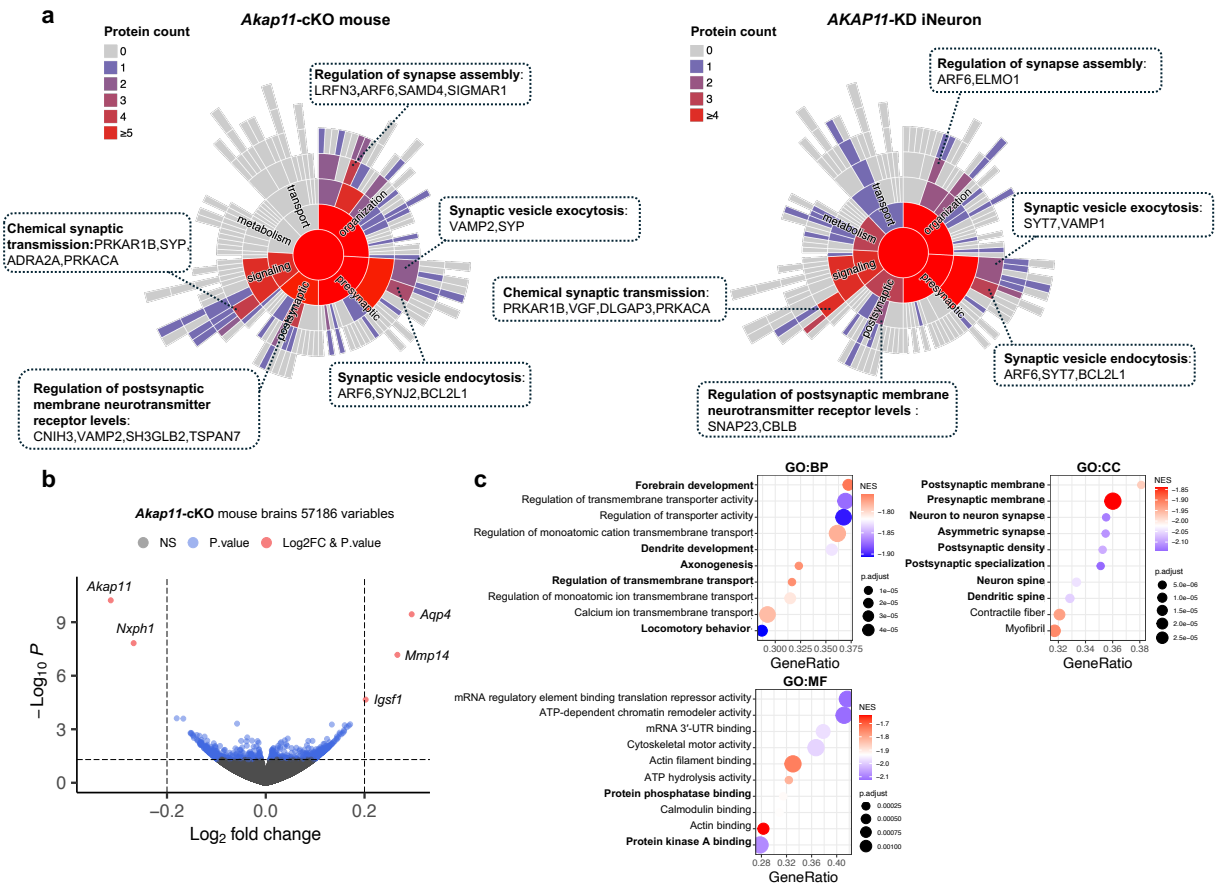

Extended Data Fig. 2: Synapse protein enrichment and transcriptomic analysis of brain lysate from *AKAP11*-deficient neurons.

a, Sunburst plots depicting SynGO Biological Process pathways with a *P*-value < 0.05. For selected ontologies, representative DEPs in the ontology are displayed.

b, Volcano plot of the differentially expressed genes (DEGs) in *Akap11*-cKO mouse brains. A positive score indicates enrichment, a negative score indicates depletion. The y axis represents statistical confidence (adjust *P*-value) for each x axis point. Enriched genes, defined by having adjusted *P*-value < 0.05 and Log2FC > 0.2, are colored in red.

c, Gene set enrichment analysis (GSEA) of all protein Gene set enrichment analysis of all proteins displayed in **a**, showing the top 10 ontologies with a negative normalized enrichment score (NES) and adjusted *P*-value < 0.05.

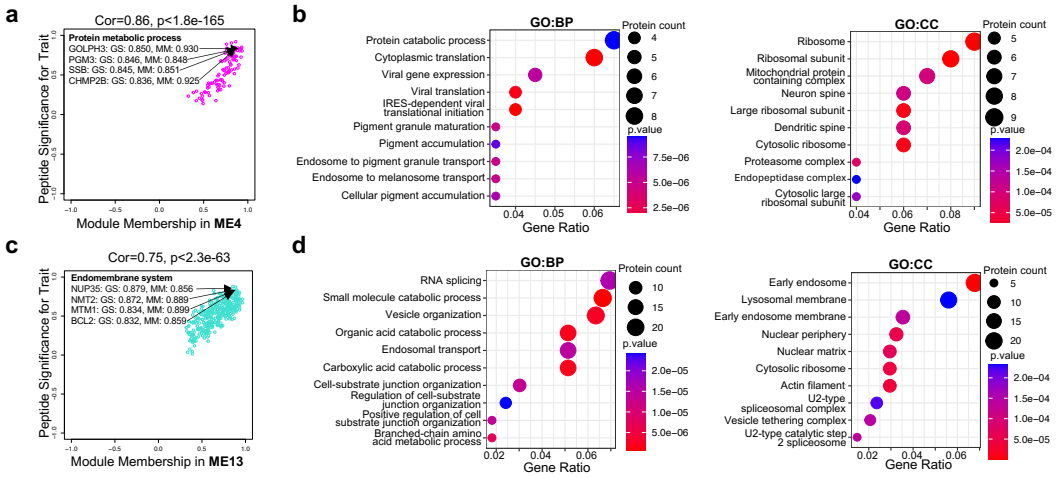

Extended Data Fig. 3: Identification of co-regulation of cellular pathways in positive corelated protein modules upon *AKAP11*-deficiency through WGCNA.

a,**c**, Scatter plot of the module membership (X axis) and peptide significance (Y axis) in ME4 from *Akap11*-cKO mouse brains (**a**) or ME13 from *AKAP11*-KD from human iNeurons (**c**).

b,**d**, Gene Ontology (GO) annotations of the proteins in ME4 from *Akap11*-cKO mouse brains (**b**) or ME13 from *AKAP11*-KD from human iNeurons (**d**), showing top 10 enriched pathways with *P*-value < 0.05.

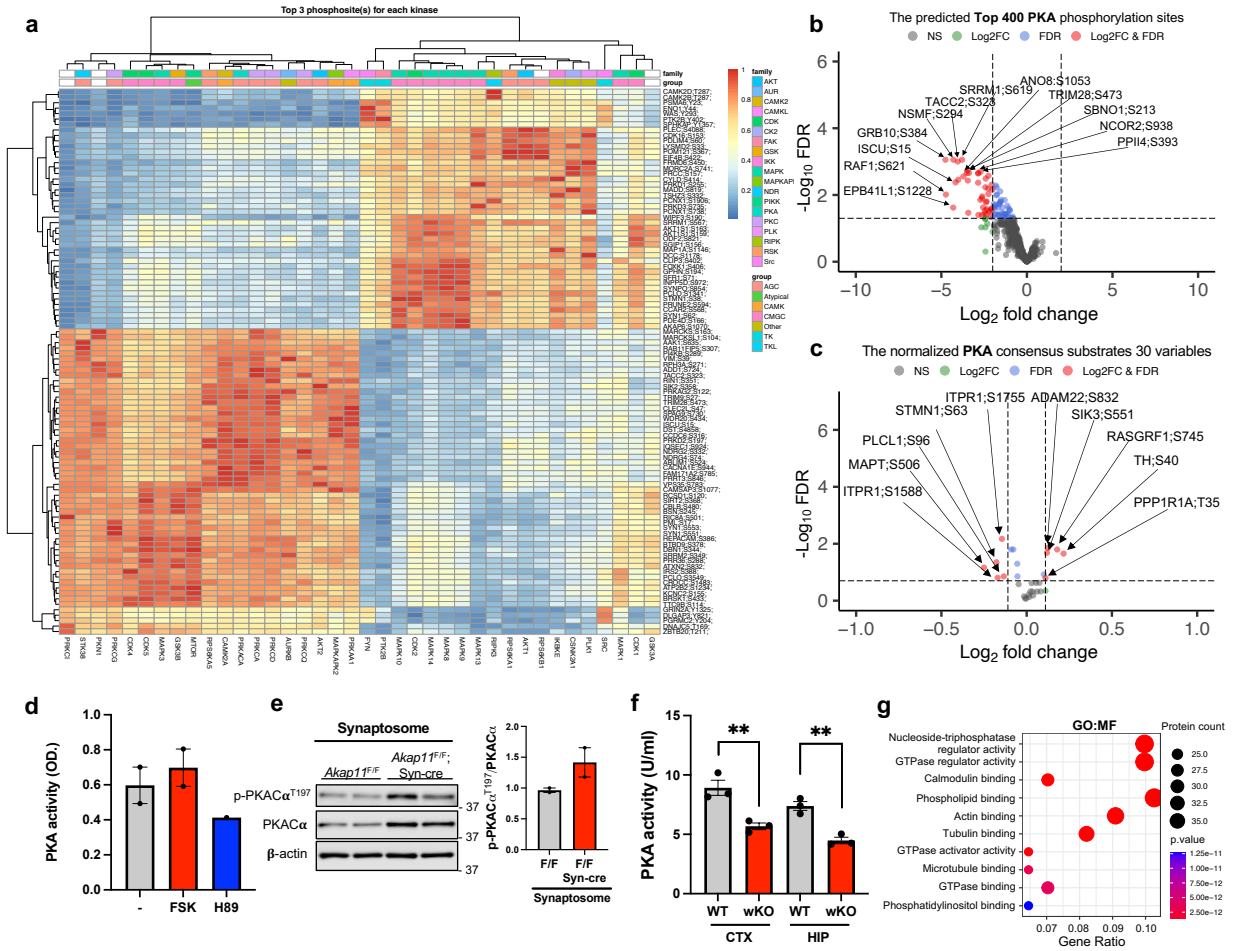

Extended Data Fig. 4: Exploration of altered kinase activities in *Akap11*-cKO brain lysates.

a, Heatmap of the top three phosphoprotein sites for each kinase. The differentially abundant phosphoprotein sites (y axis) and the kinases (x axis) are plotted.

b, Volcano plot of the top 400 predicted PKA phosphorylation sites detected by mass-spectrometry in *Akap11*-cKO mouse brains. A positive score indicates enrichment, a negative score indicates depletion. The y axis represents statistical confidence (adjusted *P*-value (FDR)) for each x axis point. Enriched proteins, defined by FDR < 0.05 and Log2FC > 2SD, are colored in red.

c, Volcano plot of the PKA consensus substrates (normalized by the total protein level) detected by mass-spectrometry in *Akap11*-cKO mouse brains. A positive score indicates enrichment, a negative score indicates depletion. The y axis represents statistical confidence (adjusted *P*-value (FDR)) for each x axis point. Enriched proteins, defined by having FDR < 0.1 and Log2FC > SD, are colored in red.

1098 **d**, Bar graph of the results from the ELISA of PKA activity from primary neurons treated with
1099 10μM forskolin (FSK) or 5μM H89 treatment for 30 minutes. Data are presented as mean ±
1100 SEM.

1101 **e**, Immunoblotting using antibodies against PKACα and p-PKACα^{T197} in synaptosome fraction
1102 and quantification of the results. Data are presented as mean ± SEM. Statistical analysis was
1103 performed using an unpaired *t*-test.

1104 **f,** Bar graph of the results from the ELISA of PKA activity in the cytosolic fraction of the
1105 cerebral cortex and hippocampus of *Akap11*-wKO mice. Brain tissues were homogenized in
1106 50mM Tris-HCl (pH 7.5), 0.32M sucrose, 1mM $MaCl_2$, 2.5mM $CaCl_2$, and 1mM NaCl before
1107 analysis. Data are presented as mean ± SEM (n=3 per genotype). Statistical analysis was
1108 performed using an unpaired *t*-test.

1109 **g,** Gene Ontology (GO) annotations of the predicted PKA substrates in **Fig. 3g**, displaying the
1110 top 10 enriched pathways with *P*-value < 0.05.

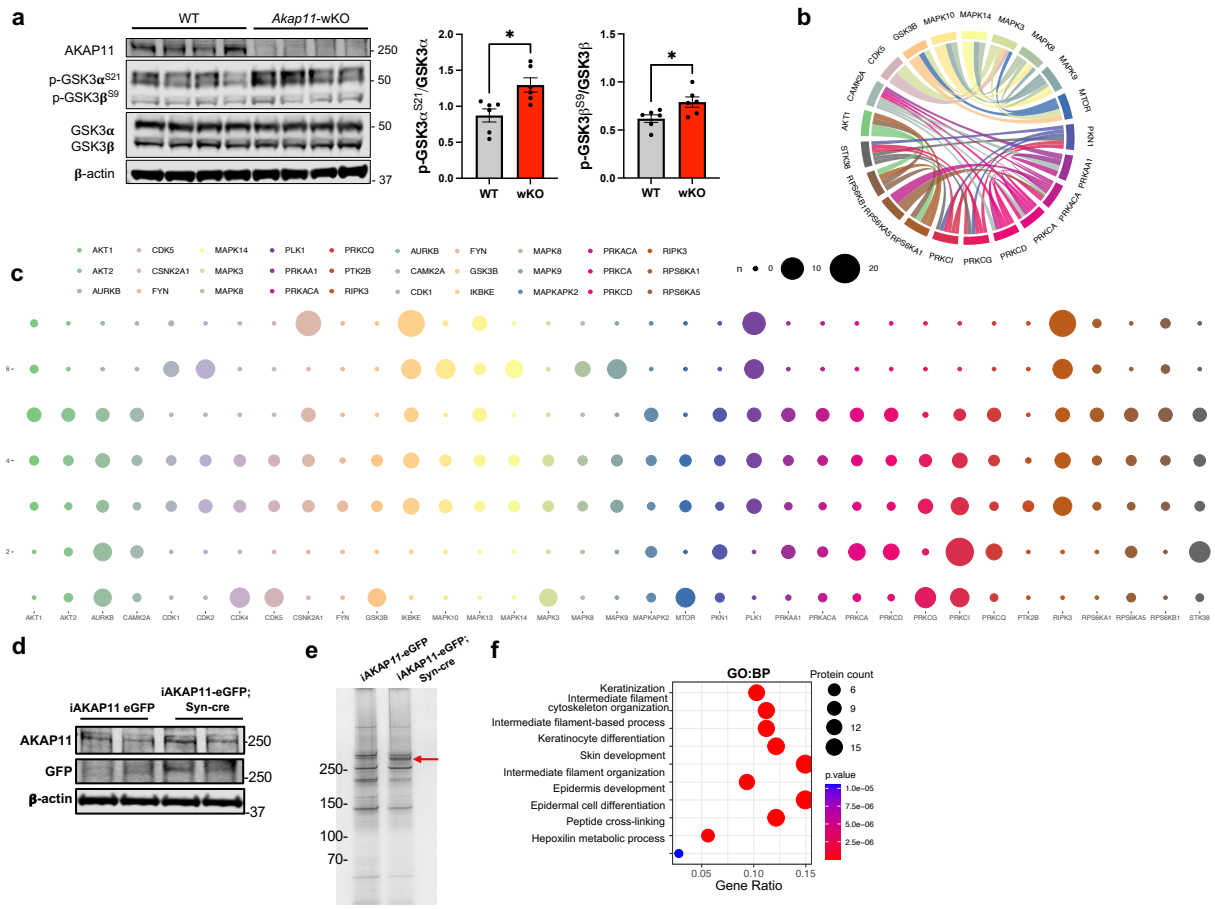

Extended Data Fig. 5 Exploration of kinase network and pattern.

a, Immunoblotting using antibodies against AKAP11, GSK3α/β and p-GSK3α/β(S21/S9) and quantification of the blot results. Data are presented as mean ± SEM (n=6 per genotype). Statistical analysis was performed using an unpaired *t*-test.

b, Kinase network analysis of all detected kinases in *Akap11*-cKO mouse brains. The nodes represent kinases; the edges refer to the *Pearson*'s correlation of kinase regulation between the two nodes. The wider the edge, the stronger the correlation.

c, Balloon plot of the patterns for each kinase. The y-axis represents the distribution of the predicted substrates in seven protein modules for each kinase (x-axis).

d, Immunoblotting using antibodies against AKAP11, GFP and β-actin.

e, Silver stained SDS-PAGE for IP samples from cytoplasm of AKAP11-eGFP and AKAP11-eGFP; Syn-cre mouse brains. 10% of the IP sample was loaded from each IP sample. Arrow indicated IP-ed AKAP11-eGFP protein.

1125 **f**, Gene Ontology (GO) annotations of the proteins shown in **Fig. 5f**, displaying the top 10
1126 enriched pathways with *P*-value < 0.05.

1127

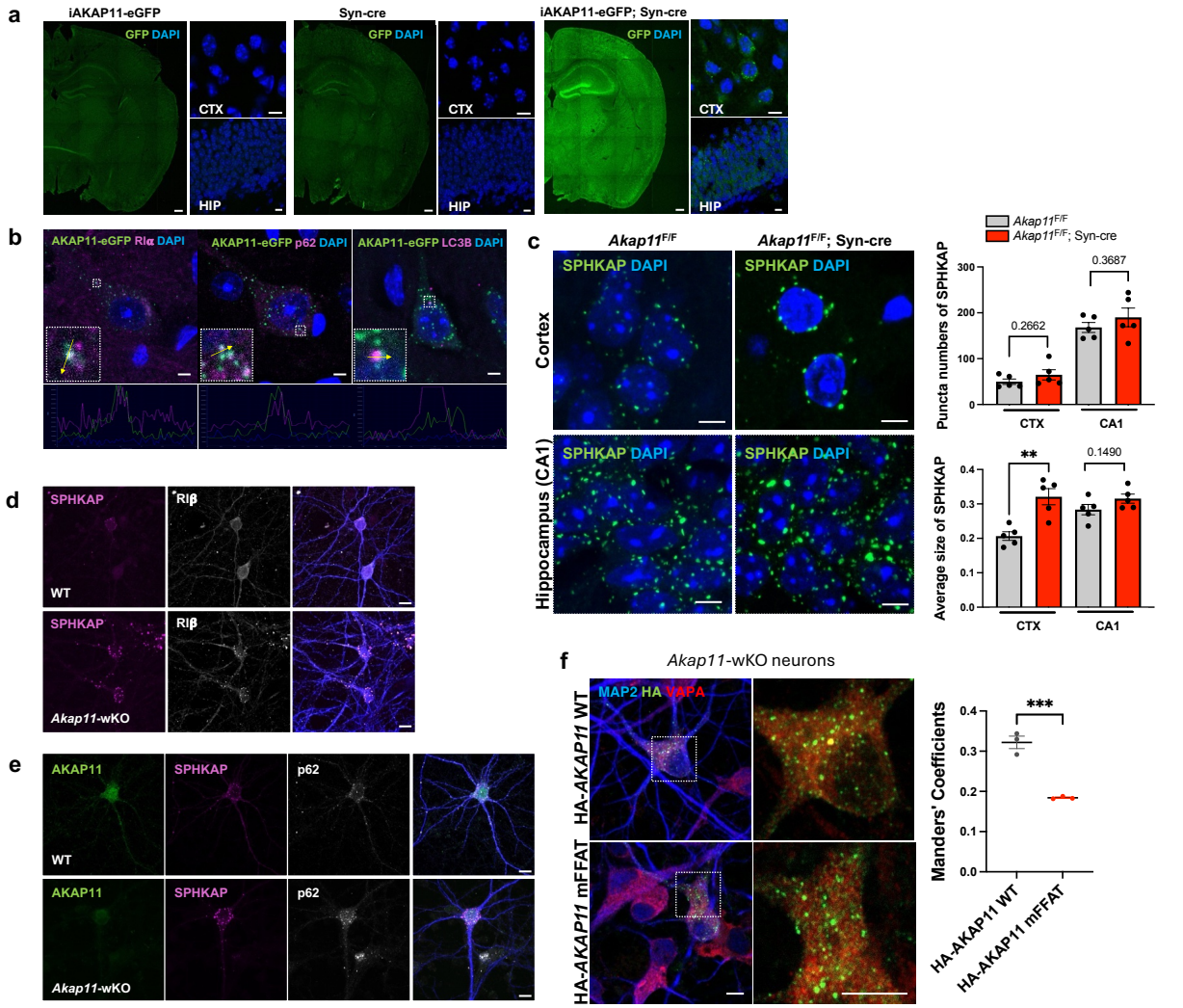

Extended Data Fig. 6: Characterization of SPHKAP in neurons from *Akap11*-cKO mouse brains.

a, Immunofluorescence images of cortical sections from AKAP11-eGFP, Syn-cre, and AKAP11-eGFP; Syn-cre mice brain, showing AKAP11 expression in overall brain regions. Inset images provide magnified views of cortex and hippocampus. Scale bars, 200µm (main images); 10µm (inset images).

b, Representative immunofluorescence images of AKAP11-eGFP transgenic mice brain slices stained with anti-RIα and anti-VAPB antibodies in the cortex, showing co-localization of these proteins. Scale bars, 5µm.

c, Immunofluorescence images of *Akap11*$^{F/F}$ and *Akap11*$^{F/F}$ Syn-cre mice brain stained with anti-SPHKAP antibody. Scale bars, 5µm. Quantification of SPHKAP puncta numbers and average size using Analyze Particles in ImageJ. Data are presented as mean ± SEM. Statistical significance (**$p<0.01$) was performed using an unpaired t-test.

1142 **d**, Immunofluorescence images of primary neuron from WT and *Akap11*-wKO mice stained with
1143 anti-SPHKAP, anti-RIβ, and anti-MAP2 antibodies. Scale bars, 10μm.

1144 **e**, Immunofluorescence images of primary neuron from WT and *Akap11*-wKO mice stained with
1145 anti-AKAP11, anti-SPHKAP, anti-p62, anti-MAP2 antibodies. Scale bars, 10μm.

1146 **f,** Primary neurons from *Akap11*-wKO mice expressing HA-AKAP11 WT or mFFAT were
1147 stained with antibodies against HA, VAPA, and MAP2. The bar graph shows quantification of
1148 HA–VAPA co-localized signal using Manders' coefficient. Data are presented as mean ± SEM
1149 (n > 3 per group). Statistical significance (***$p<0.001$) was performed using an unpaired *t*-test.
1150 Scale bars, 5 μm.

1151

1152

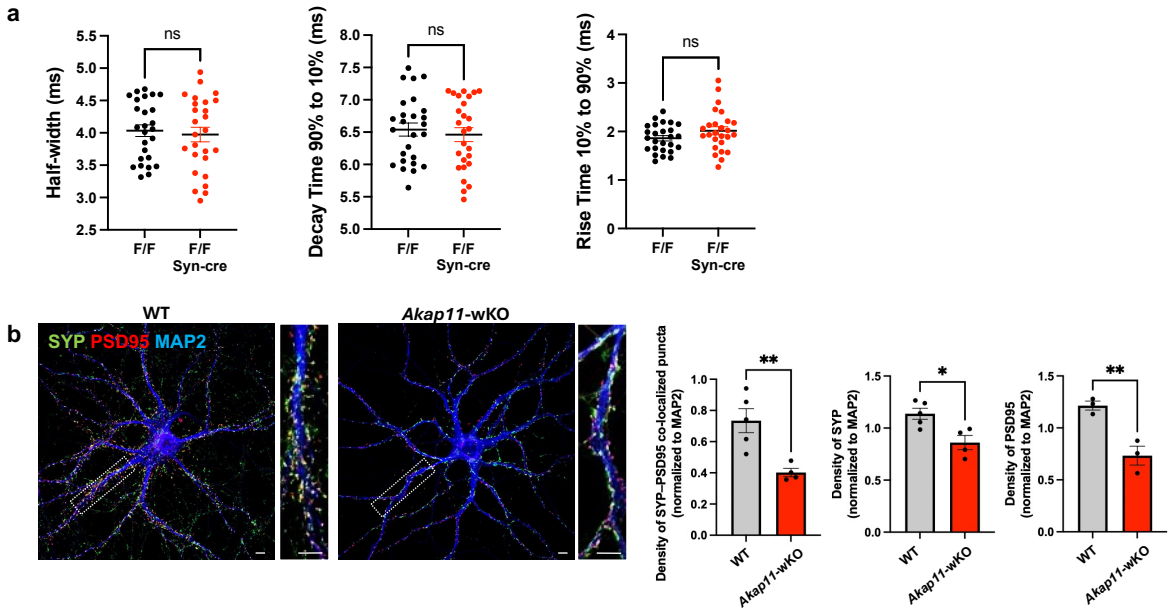

Extended Data Fig. 7: Impaired spontaneous neurotransmitter release in *AKAP11*-deficient neurons.

a, Quantification of mEPSC kinetics in the PFC of *Akap11*$^{F/F}$ and *Akap11*$^{F/F}$; Syn-cre brain slices. Kinetic parameters include half-width (duration at 50% of peak amplitude), decay time (time to decay from 90% to 10% of peak), and rise time (time to rise from 10% to 90% of the peak). Data are presented as mean ± SEM (n>26 neurons, 3 independent replicates). Statistical significance was performed using an unpaired *t*-test.

b, Immunofluorescence imaging and quantification of the WT and *Akap11*-wKO stained with anti-Synaptophysin, anti-PSD95, and anti-MAP2. Scale bars, 5µm. The bar graph shows quantification of puncta number per µm^2 neurite. Data are presented as mean ± SEM (n>4 per genotype). Statistical analysis was performed using an unpaired *t*-test (*p<0.05, **p<0.01, and ***p<0.001).

1166 **REFERENCES**

1167 1. Palmer, D. S. *et al.* Exome sequencing in bipolar disorder identifies AKAP11 as a risk gene
1168 shared with schizophrenia. *Nat. Genet.* **54**, 541–547 (2022).
1169 2. Liu, D. *et al.* Schizophrenia risk conferred by rare protein-truncating variants is conserved
1170 across diverse human populations. *Nat. Genet.* **55**, 369–376 (2023).
1171 3. Singh, T. *et al.* Rare coding variants in ten genes confer substantial risk for schizophrenia.
1172 *Nature* **604**, 509–516 (2022).
1173 4. Lester, L. B., Coghlan, V. M., Nauert, B. & Scott, J. D. Cloning and Characterization of a
1174 Novel A-kinase Anchoring Protein. *J. Biol. Chem.* **271**, 9460–9465 (1996).
1175 5. Whiting, J. L. *et al.* Protein Kinase A Opposes the Phosphorylation-dependent Recruitment
1176 of Glycogen Synthase Kinase 3β to A-kinase Anchoring Protein 220. *J. Biol. Chem.* **290**,
1177 19445–19457 (2015).
1178 6. Fang, X. *et al.* Phosphorylation and inactivation of glycogen synthase kinase 3 by protein
1179 kinase A. *Proc. Natl. Acad. Sci.* **97**, 11960–11965 (2000).
1180 7. Tanji, C. *et al.* A-Kinase Anchoring Protein AKAP220 Binds to Glycogen Synthase Kinase-
1181 3β (GSK-3β) and Mediates Protein Kinase A-dependent Inhibition of GSK-3β. *J. Biol.*
1182 *Chem.* **277**, 36955–36961 (2002).
1183 8. Wong, W. & Scott, J. D. AKAP signalling complexes: focal points in space and time. *Nat.*
1184 *Rev. Mol. Cell Biol.* **5**, 959–970 (2004).
1185 9. Deng, Z. *et al.* Selective autophagy of AKAP11 activates cAMP/PKA to fuel mitochondrial
1186 metabolism and tumor cell growth. *Proc. Natl. Acad. Sci.* **118**, e2020215118 (2021).
1187 10. Zhou, X. *et al.* Integrated proteomics reveals autophagy landscape and an autophagy receptor
1188 controlling PKA-RI complex homeostasis in neurons. *Nat. Commun.* **15**, 3113 (2024).

1189 11. Herzog, L. E. *et al.* Mouse mutants in schizophrenia risk genes GRIN2A and AKAP11 show
1190 EEG abnormalities in common with schizophrenia patients. *Transl. Psychiatry* **13**, 92 (2023).
1191 12. Aryal, S. *et al.* Deep proteomics identifies shared molecular pathway alterations in synapses
1192 of patients with schizophrenia and bipolar disorder and mouse model. *Cell Rep.* **42**, 112497
1193 (2023).
1194 13. Kallergi, E. *et al.* Dendritic autophagy degrades postsynaptic proteins and is required for
1195 long-term synaptic depression in mice. *Nat. Commun.* **13**, 680 (2022).
1196 14. Ji, C., Tang, M., Zeidler, C., Höhfeld, J. & Johnson, G. V. BAG3 and SYNPO (synaptopodin)
1197 facilitate phospho-MAPT/Tau degradation via autophagy in neuronal processes. *Autophagy*
1198 **15**, 1199–1213 (2019).
1199 15. Chang, Y.-C. *et al.* Identification of secretory autophagy as a mechanism modulating
1200 activity-induced synaptic remodeling. *Proc. Natl. Acad. Sci.* **121**, e2315958121 (2024).
1201 16. Nikoletopoulou, V., Sidiropoulou, K., Kallergi, E., Dalezios, Y. & Tavernarakis, N.
1202 Modulation of Autophagy by BDNF Underlies Synaptic Plasticity. *Cell Metab.* **26**, 230-
1203 242.e5 (2017).
1204 17. Zhang, X. *et al.* Ischemia-induced upregulation of autophagy preludes dysfunctional
1205 lysosomal storage and associated synaptic impairments in neurons. *Autophagy* **17**, 1519–
1206 1542 (2021).
1207 18. Lieberman, O. J. & Sulzer, D. The Synaptic Autophagy Cycle. *J. Mol. Biol.* **432**, 2589–2604
1208 (2020).
1209 19. Tomoda, T., Yang, K. & Sawa, A. Neuronal Autophagy in Synaptic Functions and Psychiatric
1210 Disorders. *Biol. Psychiatry* **87**, 787–796 (2020).
1211 20. Wang, Z. *et al.* 27-Plex Tandem Mass Tag Mass Spectrometry for Profiling Brain Proteome
1212 in Alzheimer's Disease. *Anal. Chem.* **92**, 7162–7170 (2020).

1213 21. Bai, B. *et al.* Deep Profiling of Proteome and Phosphoproteome by Isobaric Labeling,
1214 Extensive Liquid Chromatography, and Mass Spectrometry. in *Methods in Enzymology* (ed.
1215 Shukla, A. K.) vol. 585 377–395 (Academic Press, 2017).
1216 22. Ctortecka, C. *et al.* Comparative Proteome Signatures of Trace Samples by Multiplexed
1217 Data-Independent Acquisition. *Mol. Cell. Proteomics* **21**, (2022).
1218 23. Xu, S. *et al.* Using clusterProfiler to characterize multiomics data. *Nat. Protoc.* **19**, 3292–
1219 3320 (2024).
1220 24. Zhu, J. *et al.* Tumour immune rejection triggered by activation of α2-adrenergic receptors.
1221 *Nature* **618**, 607–615 (2023).
1222 25. Zhao, X., Zhang, Y., Zuo, X., Wang, S. & Dong, X. Knockdown of Adra2a Increases
1223 Secretion of Growth Factors and Wound Healing Ability in Diabetic Adipose-Derived Stem
1224 Cells. *Stem Cells Int.* **2022**, 5704628 (2022).
1225 26. Ali, S. & Dwivedi, Y. Early-Life Stress Influences the Transcriptional Activation of Alpha-
1226 2A Adrenergic Receptor and Associated Protein Kinase A Signaling Molecules in the Frontal
1227 Cortex of Rats. *Mol. Neurobiol.* (2024).
1228 27. Sadeghi, M. A. *et al.* Phosphodiesterase inhibitors in psychiatric disorders.
1229 *Psychopharmacology (Berl.)* **240**, 1201–1219 (2023).
1230 28. Kashiwagi, E. *et al.* Downregulation of phosphodiesterase 4B (PDE4B) activates protein
1231 kinase A and contributes to the progression of prostate cancer. *The Prostate* **72**, 741–751
1232 (2012).
1233 29. Kähler, A. K. *et al.* Association study of PDE4B gene variants in Scandinavian schizophrenia
1234 and bipolar disorder multicenter case-control samples. *Am. J. Med. Genet. Part B*
1235 *Neuropsychiatr. Genet. Off. Publ. Int. Soc. Psychiatr. Genet.* **153B**, 86–96 (2010).

1236 30. Chung, S. *et al.* Overexpressing PKIB in prostate cancer promotes its aggressiveness by
1237 linking between PKA and Akt pathways. *Oncogene* **28**, 2849–2859 (2009).
1238 31. Kovanich, D. *et al.* Sphingosine Kinase Interacting Protein is an A-Kinase Anchoring Protein
1239 Specific for Type I cAMP-Dependent Protein Kinase. *ChemBioChem* **11**, 963–971 (2010).
1240 32. Shaywitz, A. J. & Greenberg, M. E. CREB: A Stimulus-Induced Transcription Factor
1241 Activated by A Diverse Array of Extracellular Signals. *Annu. Rev. Biochem.* **68**, 821–861
1242 (1999).
1243 33. Thiel, G. Synapsin I, synapsin II, and synaptophysin: marker proteins of synaptic vesicles.
1244 *Brain Pathol. Zurich Switz.* **3**, 87–95 (1993).
1245 34. Hudmon, A. & Schulman, H. Neuronal CA2+/calmodulin-dependent protein kinase II: the
1246 role of structure and autoregulation in cellular function. *Annu. Rev. Biochem.* **71**, 473–510
1247 (2002).
1248 35. Koopmans, F. *et al.* SynGO: An Evidence-Based, Expert-Curated Knowledge Base for the
1249 Synapse. *Neuron* **103**, 217-234.e4 (2019).
1250 36. Subramanian, A. *et al.* Gene set enrichment analysis: A knowledge-based approach for
1251 interpreting genome-wide expression profiles. *Proc. Natl. Acad. Sci.* **102**, 15545–15550
1252 (2005).
1253 37. Mootha, V. K. *et al.* PGC-1α-responsive genes involved in oxidative phosphorylation are
1254 coordinately downregulated in human diabetes. *Nat. Genet.* **34**, 267–273 (2003).
1255 38. Piñero, J. *et al.* The DisGeNET knowledge platform for disease genomics: 2019 update.
1256 *Nucleic Acids Res.* **48**, D845–D855 (2020).
1257 39. Langfelder, P. & Horvath, S. WGCNA: an R package for weighted correlation network
1258 analysis. *BMC Bioinformatics* **9**, 559 (2008).

1259 40. Pei, G., Chen, L. & Zhang, W. WGCNA Application to Proteomic and Metabolomic Data
1260 Analysis. in *Methods in Enzymology* vol. 585 135–158 (Elsevier, 2017).
1261 41. Szklarczyk, D. *et al.* The STRING database in 2023: protein-protein association networks
1262 and functional enrichment analyses for any sequenced genome of interest. *Nucleic Acids Res.*
1263 **51**, D638–D646 (2023).
1264 42. Yu, Y. *et al.* Developmental regulation of tau phosphorylation, tau kinases, and tau
1265 phosphatases. *J. Neurochem.* **108**, 1480–1494 (2009).
1266 43. Li, H., Adamik, R., Pacheco-Rodriguez, G., Moss, J. & Vaughan, M. Protein kinase A-
1267 anchoring (AKAP) domains in brefeldin A-inhibited guanine nucleotide-exchange protein 2
1268 (BIG2). *Proc. Natl. Acad. Sci.* **100**, 1627–1632 (2003).
1269 44. Kuroda, F., Moss, J. & Vaughan, M. Regulation of brefeldin A-inhibited guanine nucleotide-
1270 exchange protein 1 (BIG1) and BIG2 activity via PKA and protein phosphatase 1γ. *Proc.*
1271 *Natl. Acad. Sci.* **104**, 3201–3206 (2007).
1272 45. Yoon, S., Piguel, N. H. & Penzes, P. Roles and mechanisms of ankyrin-G in neuropsychiatric
1273 disorders. *Exp. Mol. Med.* **54**, 867–877 (2022).
1274 46. Brauchle, M. *et al.* Protein Complex Interactor Analysis and Differential Activity of KDM3
1275 Subfamily Members Towards H3K9 Methylation. *PLOS ONE* **8**, e60549 (2013).
1276 47. Signorile, A. *et al.* cAMP/PKA Signaling Modulates Mitochondrial Supercomplex
1277 Organization. *Int. J. Mol. Sci.* **23**, 9655 (2022).
1278 48. Sunitha, B. *et al.* Human muscle pathology is associated with altered phosphoprotein profile
1279 of mitochondrial proteins in the skeletal muscle. *J. Proteomics* **211**, 103556 (2020).
1280 49. Zhong, J., Dong, J., Ruan, W. & Duan, X. Potential Theranostic Roles of SLC4 Molecules in
1281 Human Diseases. *Int. J. Mol. Sci.* **24**, 15166 (2023).

1282 50. Peña-Münzenmayer, G. *et al.* Activation of the Ae4 (Slc4a9) cation-driven Cl−/HCO3−
1283 exchanger by the cAMP-dependent protein kinase in salivary gland acinar cells. *Am. J.*
1284 *Physiol.-Gastrointest. Liver Physiol.* **321**, G628–G638 (2021).
1285 51. Kim, H. J., Kim, T., Xiao, D. & Yang, P. Protocol for the processing and downstream
1286 analysis of phosphoproteomic data with PhosR. *STAR Protoc.* **2**, 100585 (2021).
1287 52. Hornbeck, P. V. *et al.* PhosphoSitePlus, 2014: mutations, PTMs and recalibrations. *Nucleic*
1288 *Acids Res.* **43**, D512–D520 (2015).
1289 53. Kim, H. J. *et al.* PhosR enables processing and functional analysis of phosphoproteomic
1290 data. *Cell Rep.* **34**, 108771 (2021).
1291 54. Fang, X.-L. *et al.* Suppression of cAMP/PKA/CREB signaling ameliorates retinal injury in
1292 diabetic retinopathy. *Kaohsiung J. Med. Sci.* **39**, 916–926 (2023).
1293 55. Yu, L. *et al.* Atorvastatin inhibits neuronal apoptosis via activating cAMP/PKA/p-
1294 CREB/BDNF pathway in hypoxic-ischemic neonatal rats. *FASEB J.* **36**, e22263 (2022).
1295 56. Sarbassov, D. D., Guertin, D. A., Ali, S. M. & Sabatini, D. M. Phosphorylation and
1296 Regulation of Akt/PKB by the Rictor-mTOR Complex. *Science* **307**, 1098–1101 (2005).
1297 57. Cross, D. A. E., Alessi, D. R., Cohen, P., Andjelkovich, M. & Hemmings, B. A. Inhibition of
1298 glycogen synthase kinase-3 by insulin mediated by protein kinase B. *Nature* **378**, 785–789
1299 (1995).
1300 58. Nishimura, T. & Tooze, S. A. Emerging roles of ATG proteins and membrane lipids in
1301 autophagosome formation. *Cell Discov.* **6**, 1–18 (2020).
1302 59. Zhao, Y. G. *et al.* The ER Contact Proteins VAPA/B Interact with Multiple Autophagy
1303 Proteins to Modulate Autophagosome Biogenesis. *Curr. Biol.* **28**, 1234-1245.e4 (2018).
1304 60. Vierra, N. C. *et al.* Neuronal ER-plasma membrane junctions couple excitation to Ca2+-
1305 activated PKA signaling. *Nat. Commun.* **14**, 5231 (2023).

1306 61. Vierra, N. C. Compartmentalized signaling in the soma: Coordination of electrical and
1307 protein kinase A signaling at neuronal ER-plasma membrane junctions. *BioEssays* **46**,
1308 2400126 (2024).
1309 62. Kamemura, K. & Chihara, T. Multiple functions of the ER-resident VAP and its extracellular
1310 role in neural development and disease. *J. Biochem. (Tokyo)* **165**, 391–400 (2019).
1311 63. Dong, R. *et al.* Endosome-ER Contacts Control Actin Nucleation and Retromer Function
1312 through VAP-Dependent Regulation of PI4P. *Cell* **166**, 408–423 (2016).
1313 64. Yan, Z. & Rein, B. Mechanisms of synaptic transmission dysregulation in the prefrontal
1314 cortex: pathophysiological implications. *Mol. Psychiatry* **27**, 445–465 (2022).
1315 65. Mandal, P. K. *et al.* Schizophrenia, Bipolar and Major Depressive Disorders: Overview of
1316 Clinical Features, Neurotransmitter Alterations, Pharmacological Interventions, and Impact
1317 of Oxidative Stress in the Disease Process. *ACS Chem. Neurosci.* **13**, 2784–2802 (2022).
1318 66. Smucny, J., Dienel, S. J., Lewis, D. A. & Carter, C. S. Mechanisms underlying dorsolateral
1319 prefrontal cortex contributions to cognitive dysfunction in schizophrenia.
1320 *Neuropsychopharmacology* **47**, 292–308 (2022).
1321 67. Hoseth, E. Z. *et al.* A Study of TNF Pathway Activation in Schizophrenia and Bipolar
1322 Disorder in Plasma and Brain Tissue. *Schizophr. Bull.* **43**, 881–890 (2017).
1323 68. Gao, W.-J., Yang, S.-S., Mack, N. R. & Chamberlin, L. A. Aberrant maturation and
1324 connectivity of prefrontal cortex in schizophrenia—contribution of NMDA receptor
1325 development and hypofunction. *Mol. Psychiatry* **27**, 731–743 (2022).
1326 69. Omar, M. H. & Scott, J. D. AKAP Signaling Islands: Venues for Precision Pharmacology.
1327 *Trends Pharmacol. Sci.* **41**, 933–946 (2020).

1328 70. Morgan-Smith, M., Wu, Y., Zhu, X., Pringle, J. & Snider, W. D. GSK-3 signaling in
1329 developing cortical neurons is essential for radial migration and dendritic orientation. *eLife* **3**,
1330 e02663 (2014).
1331 71. Valvezan, A. J. & Klein, P. S. GSK-3 and Wnt Signaling in Neurogenesis and Bipolar
1332 Disorder. *Front. Mol. Neurosci.* **5**, (2012).
1333 72. Jope, R. S. & Roh, M.-S. Glycogen Synthase Kinase-3 (GSK3) in Psychiatric Diseases and
1334 Therapeutic Interventions. *Curr. Drug Targets* **7**, 1421–1434 (2006).
1335 73. Zhou, X., Wang, H., Burg, M. B. & Ferraris, J. D. Inhibitory phosphorylation of GSK-3β by
1336 AKT, PKA, and PI3K contributes to high NaCl-induced activation of the transcription factor
1337 NFAT5 (TonEBP/OREBP). *Am. J. Physiol.-Ren. Physiol.* **304**, F908–F917 (2013).
1338 74. Jensen, J., Brennesvik, E. O., Lai, Y.-C. & Shepherd, P. R. GSK-3β regulation in skeletal
1339 muscles by adrenaline and insulin: Evidence that PKA and PKB regulate different pools of
1340 GSK-3. *Cell. Signal.* **19**, 204–210 (2007).
1341 75. Peretti, D., Dahan, N., Shimoni, E., Hirschberg, K. & Lev, S. Coordinated Lipid Transfer
1342 between the Endoplasmic Reticulum and the Golgi Complex Requires the VAP Proteins and
1343 Is Essential for Golgi-mediated Transport. *Mol. Biol. Cell* **19**, 3871–3884 (2008).
1344 76. James, C. & Kehlenbach, R. H. The Interactome of the VAP Family of Proteins: An
1345 Overview. *Cells* **10**, 1780 (2021).
1346 77. Kors, S., Costello, J. L. & Schrader, M. VAP Proteins – From Organelle Tethers to
1347 Pathogenic Host Interactors and Their Role in Neuronal Disease. *Front. Cell Dev. Biol.* **10**,
1348 (2022).
1349 78. Bolger, A. M., Lohse, M. & Usadel, B. Trimmomatic: a flexible trimmer for Illumina
1350 sequence data. *Bioinformatics* **30**, 2114–2120 (2014).

1351 79. Kim, D., Paggi, J. M., Park, C., Bennett, C. & Salzberg, S. L. Graph-based genome
1352 alignment and genotyping with HISAT2 and HISAT-genotype. *Nat. Biotechnol.* **37**, 907–915
1353 (2019).
1354 80. Love, M. I., Huber, W. & Anders, S. Moderated estimation of fold change and dispersion for
1355 RNA-seq data with DESeq2. *Genome Biol.* **15**, 550 (2014).
1356 81. Dejanovic, B. *et al.* Complement C1q-dependent excitatory and inhibitory synapse
1357 elimination by astrocytes and microglia in Alzheimer's disease mouse models. *Nat. Aging* **2**,
1358 837–850 (2022).
1359 82. Tan, H. *et al.* Refined phosphopeptide enrichment by phosphate additive and the analysis of
1360 human brain phosphoproteome. *Proteomics* **15**, 500–507 (2015).
1361 83. Ritchie, M. E. *et al.* limma powers differential expression analyses for RNA-sequencing and
1362 microarray studies. *Nucleic Acids Res.* **43**, e47 (2015).
1363 84. Wang, X. *et al.* JUMP: a tag-based database search tool for peptide identification with high
1364 sensitivity and accuracy. *Mol. Cell. Proteomics MCP* **13**, 3663–3673 (2014).
1365 85. Shannon, P. *et al.* Cytoscape: a software environment for integrated models of biomolecular
1366 interaction networks. *Genome Res.* **13**, 2498–2504 (2003).
1367 86. Chen, J., Bardes, E. E., Aronow, B. J. & Jegga, A. G. ToppGene Suite for gene list
1368 enrichment analysis and candidate gene prioritization. *Nucleic Acids Res.* **37**, W305–W311
1369 (2009).
1370 87. Wickham, H. *Ggplot2*. (Springer International Publishing, Cham, 2016). doi:10.1007/978-3-
1371 319-24277-4.
1372 88. Blighe, K., Rana, S. & Lewis, M. EnhancedVolcano: Publication-ready volcano plots with
1373 enhanced colouring and labeling. *R Package Version* **1**, 10–18129 (2019).

89. Yang, P. *et al.* AdaSampling for Positive-Unlabeled and Label Noise Learning With Bioinformatics Applications. *IEEE Trans. Cybern.* **49**, 1932–1943 (2019).

90. Dai, J., Liakath-Ali, K., Golf, S. R. & Südhof, T. C. Distinct neurexin-cerebellin complexes control AMPA- and NMDA-receptor responses in a circuit-dependent manner. *eLife* **11**, e78649 (2022).

91. Wang, L. *et al.* Analyses of the autism-associated neuroligin-3 R451C mutation in human neurons reveal a gain-of-function synaptic mechanism. *Mol. Psychiatry* **29**, 1620–1635 (2022).